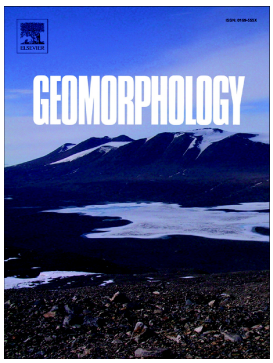


# Reconstructing the depositional history of Pleistocene fluvial deposits based on grain size, elemental geochemistry and in-situ 10Be data

Nathan Vandermaelen, Veerle Vanacker, François Clapuyt, Marcus Christl, Koen Beerten

PII: S0169-555X(22)00020-4

DOI: https://doi.org/10.1016/j.geomorph.2022.108127

Reference: GEOMOR 108127

To appear in: *Geomorphology*

Received date: 30 July 2021

Revised date: 24 January 2022

Accepted date: 24 January 2022

Please cite this article as: N. Vandermaelen, V. Vanacker, F. Clapuyt, et al., Reconstructing the depositional history of Pleistocene fluvial deposits based on grain size, elemental geochemistry and in-situ 10Be data, *Geomorphology* (2021), https://doi.org/10.1016/j.geomorph.2022.108127

# Reconstructing the depositional history of Pleistocene fluvial deposits based on grain size, elemental geochemistry and in-situ $^{10}$Be data.

Nathan Vandermaelen[a], Veerle Vanacker[a], François Clapuyt[a,c], Marcus Christl[b], Koen Beerten[d]

[a]Georges Lemaître Centre for Earth and Climate Research, Earth and Life institute, Université catholique de Louvain, Place Louis Pasteur 3, 1348 Louvain-la-Neuve, Belgium

[b]Laboratory of Ion Beam Physics, ETH Zurich, Department of Physics, Zurich, Switzerland

[c]Fonds de la Recherche Scientifique F. R. S.-FNRS, Brussels, Belgium

[d]Engineered and Geosystems Analysis, Waste and Disposal, Belgian Nuclear Research Centre SCK•CEN, Boeretang 200, 2400 Mol, Belgium

**Corresponding authors:**

nathan.vandermaelen@uclouvain.be, veerle.vanacker@uclouvain.be

**Abstract**

Constraining depositional phases in braided river deposits can be challenging if only based on sedimentology or geochronology. In this paper, we explored how different data sources can provide complementary information on the depositional history of Pleistocene fluvial deposits. The study was realized on the Zutendaal gravels that outcrop in Northeastern Belgium. In an 8 m high exposure of gravel sheets, we collected bulk samples that were processed for grain size, elemental geochemistry and cosmogenic radionuclides. After dry sieving, we derived the D10, D50, D90, gravel and sand content. From the elemental geochemistry of the bulk samples, we calculated the Ti/Zr and Cr/Zr ratios as proxies for provenance, the $Al_2O_3/SiO_2$ and Ba/Sr ratios for hydrolysis, and the MnO, $Fe_2O_3$ concentrations and the $\frac{Fe_2O_3+MnO}{Al_2O_3}$ ratio for oxidation. The $^{10}$Be concentration-depth profiles are informative to identify phases of landscape stability characterized by depositional hiatuses. To verify the existence of any aberrant variation in $^{10}$Be concentration associated to provenance, the in-situ $^{10}$Be concentrations were contrasted with provenance and weathering indices. Differences in grain size, elemental geochemistry and in-situ $^{10}$Be between sedimentary units were evaluated based on Mann-Whitney tests, while Spearman correlation tests informed us on the co-variation between data sources. The outcrop in the Zutendaal gravels contains three depositional units with significant differences in grain size and

chemical weathering extent, and representing distinct $^{10}$Be accumulation phases. The absence of correlation between provenance and oxidation proxies indicates that weathering is essentially intraformational or post-depositional. Sedimentary hiatuses were identified based on fining upward sequences and $^{10}$Be concentration-depth profiles, whereby local deviation in $^{10}$Be concentration at the top of the fining upward sequence provided information on the duration of the hiatus. The case study illustrates how co-variations in weathering, provenance, granulometry indices and $^{10}$Be concentration are informative for the depositional history of fluvial sediments, and landscape stability during the Pleistocene.

**KEYWORDS:** braided river, aggradation mode, hiatus, weathering, provenance, $^{10}$Be.

## 1. Introduction

Fluvial sediment sequences can preserve relevant information on paleo-climatic and physiographic conditions under which the sediments were deposited, and their source areas through tracing of, e.g., parent lithology (Vandenberghe, 1995; 2008; Stange et al., 2013; Lauer et al., 2020). Pioneer work by Schumm (1985) and Miall (1996) significantly improved the comprehension of the relation between sequences of gravel deposits and aggradation modes of braided rivers. More recently, major advances in the field of geochronology permitted successful dating of fluvial deposits using in-situ produced cosmogenic radionuclides (CRN) and luminescence dating (e.g., Stange et al., 2013; Claude et al., 2017; Rizza et al., 2019). However, the geochronology of braided river deposits remains challenging because of their variable deposition mode. Braided rivers are often characterized by episodic accumulation of sediment, and an alternation of phases of fluvial aggradation and non-deposition (e.g., Kemp et al., 2020). In pebbly braided rivers, channels and gravel bars can migrate laterally and the sedimentary deposits can show lateral and vertical sequences of different sedimentary facies (Collinson, 1996). Often, there is only a fraction of the sedimentary body exposed at a given location because of depositional hiatuses within and between the sequences. If long, these interruptions of deposition need to be considered when interpreting fluvial archives to infer, e.g., climate cyclicity or physiographic changes.

During periods of major fluvial activity, a characteristic sedimentary sequence consists of a series of cut-and-fill lenses of sand and gravel that extend in a parallel direction to the flow current. An aggradation cycle typically starts with a thin gravel sheet that grows downstream and upward by accumulation of clasts, fining upward as a consequence of an upward decrease of stream power. The deposition of gravels is generally followed by downstream accretion of the gravel sheet, vertical aggradation of finer sand bars and ultimately aggradation of deposits from overbank flows that further contribute to the fining upward trend (Miall, 1996). The cyclical deposition of coarse and fine-grained sediments has frequently been utilized to define boundaries between aggradation cycles (Paulissen, 1983; Miall, 1996; Bartz et al., 2017; Faust and Wolf, 2017).

Periods with high rates of fluvial activity with episodic sediment aggradation, removal and re-deposition are often followed by periods of relative quiescence. These 'dormant' intervals can represent physical discontinuities in the depositional sequence. In some cases, these breaks or hiatuses last only a few months to years when they mark the transition between cycles that are deposited seasonally (Miall, 1996). In other cases, they may last for tens of thousands of years when they are climatically controlled (Vandenberghe, 2008). During the time interval in which the surface of the hiatus is consolidated, the sediment source areas can change resulting in differences in the provenance of superposed depositional sequences. Sedimentary provenance can be analyzed based on the mineralogical and geochemical composition of detrital sediments (Kassi et al., 2015; Mitchell and Sheldon, 2016). Trace and rare earth elements, such as Zr, Hf, Nb, La, Ce and Cr, are commonly used for the discrimination of provenance. Because of their conservative geochemical behavior during sedimentary and post-depositional processes, it is commonly assumed that their element concentration reflects the signature of the source rock composition (McLennan, 2001; Hofer et al., 2013). Besides sedimentary provenance, variations in major element

compositions of sedimentary sequences can also be the result of weathering processes that transform the source rocks into solutes and newly formed minerals (Sheldon and Tabor, 2009). The extent or degree of chemical weathering is typically assessed from compositional data (Johnsson, 1993). Weathering indices, such as the chemical index of alteration (CIA), are based on the proportion of metal oxides in the sediments, and assume that monovalent and bivalent cations will preferentially be released during weathering processes (Sheldon and Tabor, 2009). If all other conditions (e.g., climate, lithology, drainage) are equal, a higher weathering extent is indicative of a longer period of exposure to weathering agents. Lateral or vertical variations in weathering extent within depositional sequences can inform us on the presence of hiatuses and their length (Miall, 1996; Retallack, 1997; 2019).

Absolute dating of Quaternary fluvial deposits is increasingly done with cosmogenic radionuclides (Schaller et al., 2001; Gosse and Philips, 2001). The cosmogenic radionuclide (CRN) $^{10}$Be forms in-situ at the earth surface during nuclear reactions between energetic particles from the cosmic rays and the constituent atoms in the Earth's crust. In constantly exposed and undisturbed sediments with no erosion, the in-situ produced $^{10}$Be concentration will increase over time with a maximum concentration at the surface. The concentration of $^{10}$Be at the surface can then be used to derive a minimum exposure age of the sediments (e.g., Akçar et al., 2017; Claude et al., 2017). Braucher et al. (2009) demonstrated that it is possible to date gravel sheets with in-situ produced cosmogenic radionuclides when the sediments are rapidly deposited and then exposed for a sufficiently long time. This concept was applied to fluvial sediments with complex aggradation history (Dehnert et al., 2011; le Dortz et al., 2012; Rizza et al., 2019). Because of the variability of the deposition processes in pebbly braided rivers, reconstructing the timing of depositional phases in such environments is often challenging (e.g., Rixhon et al., 2014) based on sedimentology or geochronology alone. By combining geochronological with geochemical and grain size data,

one can obtain a more comprehensive view on the geological and geomorphological history of fluvial deposits (Claude et al., 2017; Beerten et al., 2020).

In this paper, we therefore explore the co-variation of grain size, geochemical composition, and $^{10}$Be concentrations with depth in a fluvial gravel sheet. We hypothesize that these co-variations generate additional information on the source, depositional mode and deposition history of the Pleistocene deposits. To test this hypothesis, we proposed a conceptual framework on potential co-variations between granulometry, provenance and weathering elemental indices, and CRN concentrations. We applied this framework to pebbly braided river deposits in the Campine area (northeastern Belgium). These deposits of the river Meuse, the Zutendaal gravels, belong to the Main Terrace deposits and are considered to be Middle Pleistocene in age (van den Berg, 1996). They are an attractive case study as successional aggradational phases have been identified in the deposits (Paulissen, 1983).

## 2. Conceptual framework

In fluvial deposits that witnessed several phases of sediment aggradation, data on grain size, sediment geochemistry and cosmogenic radionuclides can provide complementary information on the fluvial aggradation history. Here, we develop for a simple sequence of two sedimentary layers, the information that we can theoretically extract on aggradation modes and rates (Fig. 1).

Grain size analyses can show uniform granulometry (a.1) or reveal fining upward or coarsening upward trends (a.2) that are indicative of fluctuating hydrodynamic conditions during net vertical aggradation (Miall, 1996). When two or more upward sequences are present, it is possible to individualize the depositional events. The geochemical

characterization of the sediments can then provide insights on their provenance and weathering. When the source of sediments does not change between two consecutive sequences, it is expected that the conservative element concentrations - used as proxies for provenance - remain uniform throughout the profile (b.1). On the contrary, changes in sediment sources can result in abrupt changes in provenance between sedimentary sequences (b.2). Measurements of ratios between major element concentrations or their oxides can give indications about chemical weathering. Weathering processes alter the chemical composition of sediments and can occur at different stages of the sedimentary cycle (Johnsson, 1993; Tebbens and Veldkamp, 2000). Pre-depositional weathering (c.1 or c.3) happens during sediment production and intermediate storage during transport towards the sink. It can be overprinted during and after deposition, which may hamper the use of weathering as a systematic tracer of, e.g., past climatic conditions (Johnsson, 1993). Between sedimentary cycles, intraformational weathering occurs when sequences are exposed for a sufficiently long time during hiatuses. Intraformational weathering (c.2) may therefore depict limits between deposition cycles separated by a period without deposition lasting at least several thousands of years (Retallack, 2019). After the aggradation phase ceases, the sediments are subject to post-depositional weathering. The development of a weathering front (c.4) is conditioned by spatio-temporal variations in water and solute fluxes throughout the profile, and redox conditions. The extent of chemical weathering, and depth variations in weathering extent, can inform us on the presence and duration of sedimentary cycles.

Cosmogenic radionuclides accumulate at the earth's surface, and the concentration increases with exposure time and decreases exponentially with depth below the surface (Granger and Muzikar, 2001). When two sedimentary sequences are deposited within a time span that is negligible compared to the time since deposition, the CRN concentration will show a single inverse exponential function with depth (d.1). Conversely, when two or more

deposition cycles are separated by a phase without deposition that is lasting more than several thousand years, the CRN concentrations will build up in the sequence during exposure (Dehnert et al., 2011; Rizza et al., 2019). If buried under a sufficiently thick overburden of more than 2 to 3 m, the oldest sedimentary sequence will partly be shielded from cosmic rays (Granger and Muzikar, 2001; Erlanger et al., 2012). A local maximum of CRN concentrations can then develop at the top of the oldest sedimentary sequence (d.2), and it can be used to derive the duration of the corresponding hiatus.

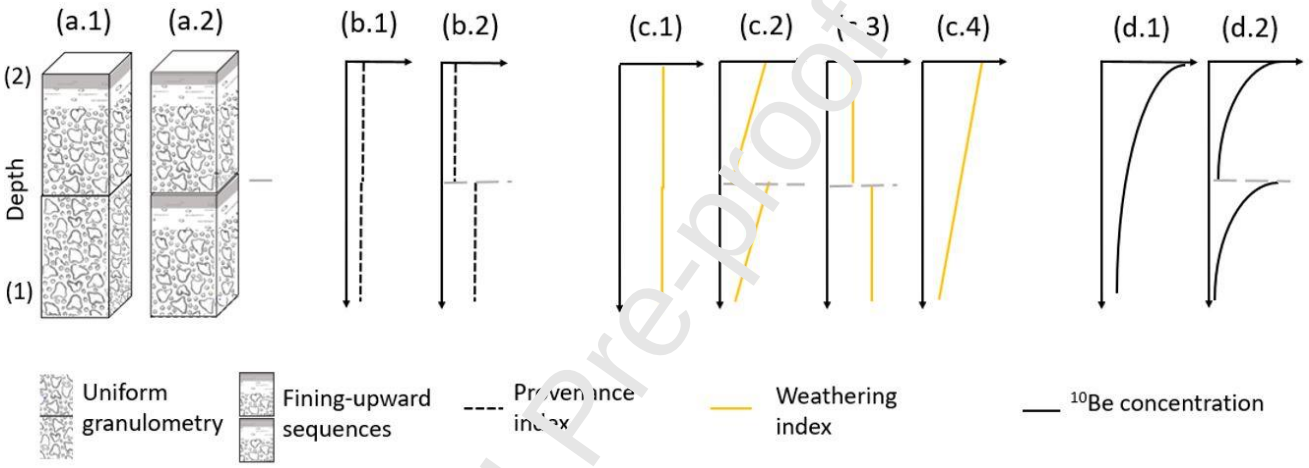


*Fig. 1. Depth variations in (a) granulometry, (b) sediment provenance, (c) weathering extent and (d) in-situ produced CRN concentrations can provide information on the depositional history of fluvial sediments.*

## 3. Geomorphological context

The Campine Plateau (northeastern Belgium) is a low-standing plateau constituted of Pleistocene fluvial deposits from the Rhine and the Meuse. It is nowadays bordered in the west by a cryopediment forming a gentle transition from the plateau to the Scheldt Basin (Fig. 2). In the southeast, the plateau is bordered by a flight of fluvial terraces of the Meuse River, that represent, in total, a 50 m difference in elevation. Towards the northwest, the Campine Plateau progressively transitions to the flat topography of the Campine area. It is bounded in the northeast by active border faults of the Roer Valley Graben, displaying a vertical topographical offset of up to 40 m (Vanneste et al., 2001).

The Zutendaal gravels (Fig. 2) cover the southeastern part of the Campine Plateau (Beerten et al., 2013). This deposit is described as a 7 to 15 m thick, medium-coarse gravel sheet, mainly consisting of material eroded from the Ardennes Massif. It follows the Winterslag sands in the lithostratigraphy. The latter two members constitute the Zutendaal Formation. Age control on the Zutendaal Formation is poor although they are commonly assumed to be Cromerian in age following the northwestern European stages (Gullentops et al., 2001). The Cromerian complex roughly coincides with the time period between 0.45 and 0.85 Ma (Cohen and Gibbard, 2011). The time period between 0.5 and 1.0 Ma was also put forward as a potential window for deposition of the Pleistocene deposits in the Campine Plateau (Laloy et al., 2017; Beerten et al., 2018).

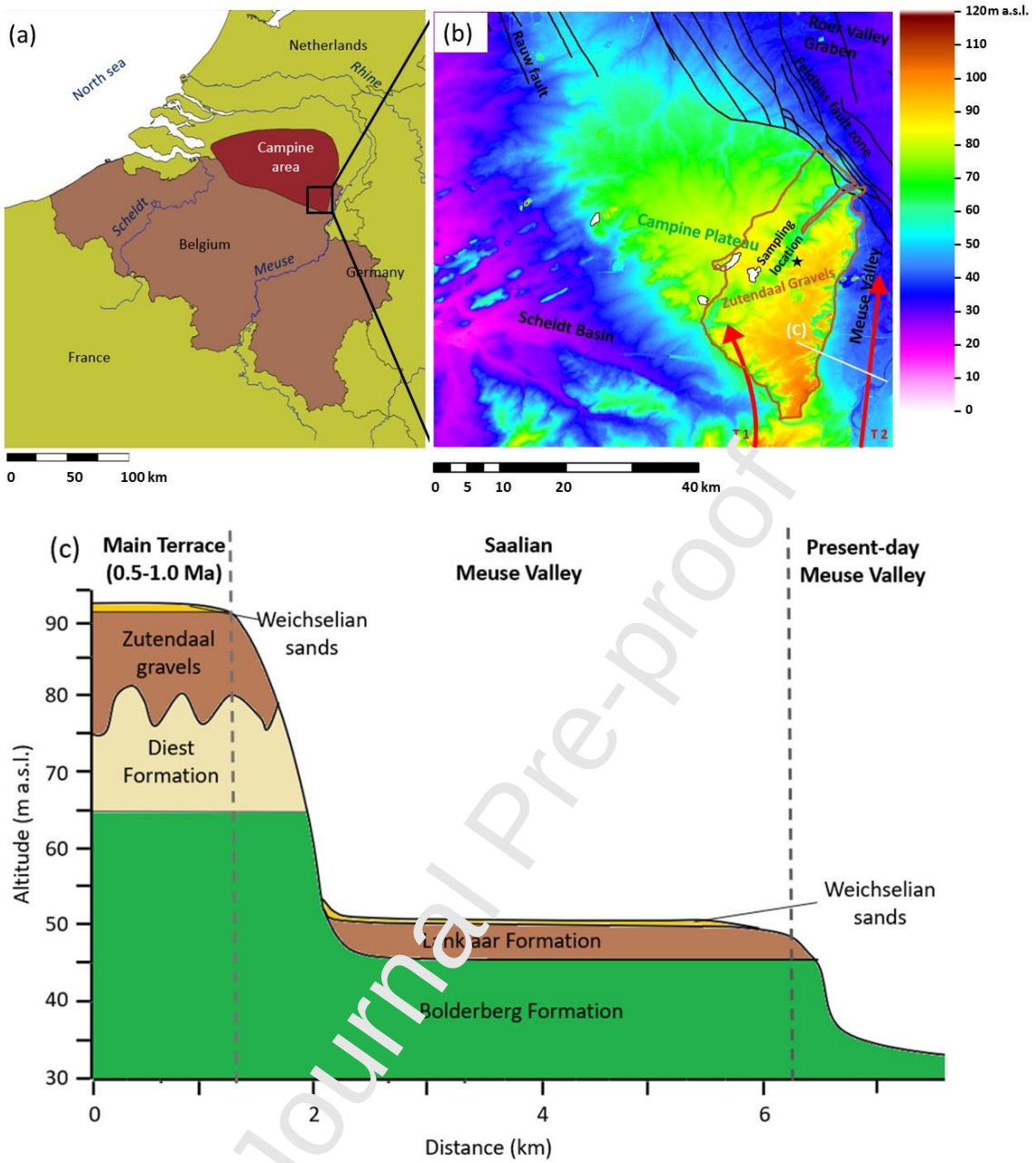


*Fig. 2. (a) The Campine area represents a region of low-laying terrain in northern Belgium and southern Netherlands. (b) The Campine Plateau reaches a maximum altitude of almost 100 m a.s.l., whereas the Campine area is generally not higher than 20 to 30 m a.s.l. The plateau gently dips towards the northwest. The Zutendaal gravels (delimited by red polygon) are present at the highest part of the plateau at its southeastern edge. (c) Transect from the eastern border of the Campine Plateau to the present-day Meuse valley (shown by a white line on panel b). The thickness of the Zutendaal gravels can vary by up to 5 m over a 100 m long section. A 40 m high escarpment marks the eastern limit of the plateau.*

The Zutendaal gravels are deposits of the Meuse River that was occupying this part of the Campine area and flowed towards the north (T1, Fig. 2). The deposition mainly occurred

under cold, periglacial climatic conditions (Paulissen, 1973), and the fluvial sediments were likely deposited by the Meuse under the form of a braided river system (Vandenberghe, 2008). The deposition is considered to have taken place over a series of aggrading cycles as identified in fining upward sequences (Paulissen, 1983). After this deposition phase, the Meuse shifted its course eastward (T2, Fig. 2) and started to incise in its own deposits leading to the stepwise development of the Meuse valley and its terrace sequence. Main steps in the terrace sequence (Fig. 2c) are the Main Terrace with the Zutendaal gravels, the Lanklaar terrace with sandy deposits of the Lanklaar Formation and the present-day Meuse valley.

Because of lower erodibility of the Zutendaal gravels in comparison to the surrounding sand deposits, the thick gravel sequences now have an elevated position on top of the Campine Plateau (Beerten et al., 2013; 2018). Several glacial-interglacial cycles occurred after the deposition of the Zutendaal Formation. At some places, there are clear indications of deep and/or intense weathering: the presence of a red-brown paleosoil (referred to as “interglacial As soil” by Gullentops et al., 2001) and concretions or coatings of Mn and Fe oxides at the base of the Zutendaal gravels (Fig. 3e and f; Dreesen et al., 2005). The Zutendaal gravels and the Lanklaar terrace are covered by Quaternary wind-dominated sandy deposits of the Gent Formation (Beerten et al., 2017).

## 4. Material and methods

### 4.1 Sampling and grain size analyses of the Zutendaal gravels

The sampling site is located in a former quarry located in the municipality of As (geosite Hermans, 51°00’29.10” N, 5°35’46.19 E, Fig. 2), where the gravel sheet reaches a thickness of more than 7 m and is exposed over more than 20 m width. The top of the profile (Fig. 2) reaches an altitude of 95 m a.s.l. The profile was described in the field: six units (U1-6) were identified based on granulometry and sorting, presence of coatings and concretions, and sedimentary structures (Fig. 3). The sand and gravel facies classification of Miall (1996) was

applied to the sequence. Thirty-seven bulk samples (> 1 kg) were taken at depths between 70 and 660 cm below the top surface, and over depth intervals of 10 cm. All 37 samples were processed for grain size determination. Of the 37 samples, fifteen samples were analysed for in-situ produced cosmogenic $^{10}$Be: the samples were selected from the top, upper middle and lower part of each unit, whereby the sampling density was highest in the upper units (U5-U6) to facilitate exposure dating. Seventeen samples were analysed for bulk geochemistry: three samples per unit were taken when possible (note that only one sample was taken in U2 that was less than 50 cm thick, Fig. 3). For elemental chemistry, samples were distributed equally over the entire thickness of the unit as to capture variation in provenance and weathering within and between the units.

After air drying, we sieved the 37 samples in a Retsch vibratory sieve shaker with 1.2 mm amplitude for 30 min. For each sample, we calculated the weight percentage of gravel (> 2 mm), medium and coarse sand (0.25 to 2 mm) and fine sand, silt and clay (< 0.25 mm). Then, the D10, D50 and D90 weight percentage statistics were obtained using Gradistat software (Blott and Pye, 2001; Vauclin et al., 2019). Weight percentages were plotted against depth, which allowed us to analyze trends in the grain size distribution (fining upward or coarsening upward sequences).

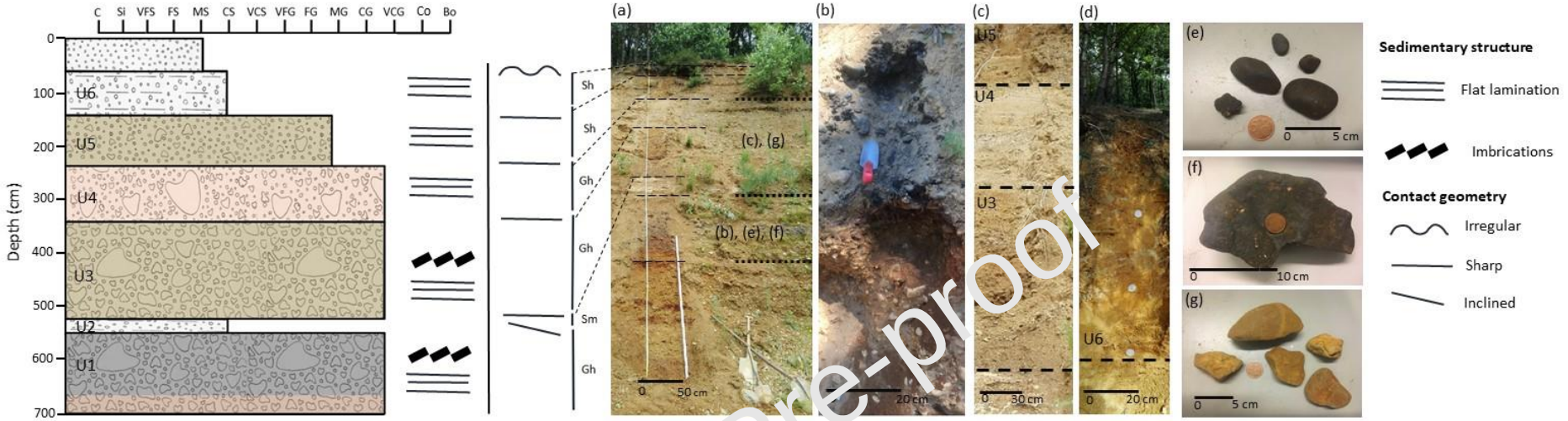


*Fig. 3. Summary of profile observations with the descriptive log (with maximum grain size per unit) and the facies classification following Miall (1996). (a) Picture of the exposure at As, with indication of location of detailed pictures (b,c, d, e, f, g). View of (b) U1, (c) U2-U5, with the thin loamy sand layer (U2) at the bottom and the gravelly sand (U5) at the top. (d) loamy sand layer (U6) covered by 60 cm of aeolian sands. (e) gravels and sandy matrix of U1 with black and brownish coatings. (f) Picture of a large angular boulder coated with Mn oxides (U1). (g) Picture of gravels sampled in U3. Note that a few, potentially ice-rafted, boulders of > 50 cm diameter were found in the former quarry, and are present at the outcrop.*

4.2 Bulk geochemistry

The bulk elemental chemistry was realized on the sand fraction (< 2 mm). We opted for this fraction because (1) the weathering signal is more noticeable in the finer fraction (Nesbitt et al., 1996; Hatano et al., 2019), and (2) for consistency with the $^{10}Be$ analyses that are typically performed on the sand fraction. A potential limitation of this approach is that the fraction above 2 mm, which represents a substantial part of most samples (see Fig. 4), is not considered for provenance and weathering. To evaluate potential bias, we verified the correlation between grain size and geochemical indices. Chemical element concentrations were determined by inductively coupled plasma-atomic emission spectrometry (Thermo iCAP 6000 Series) after the application of a lithium metaborate and tetraborate fusion of the samples at 1000°C (Chao and Sanzolone, 1992). Loss on ignition was recorded following combustion of an aliquot at 1000°C. The total element content is expressed in reference to the dry weight at 105°C. We report the concentration in major elements as oxide percentages ($K_2O$, CaO, $Na_2O$, $Fe_2O_3$, MnO, $SiO_2$ and $Al_2O_3$), and minor and trace elements in mg $kg^{-1}$ (Zr, Ba, Sr and Cr). Here, Ti was also reported in mg $kg^{-1}$ as it is analyzed in combination with Zr. The accuracy of the measurements was assessed by testing the method with the reference material BHVO-2 (Basalt, Hawaiian Volcanic Observatory, USGS). The uncertainties relative to the standard material are below 1% for all major elements and Zr, and below 5% for Ba, Sr and Cr (Table A.1).

We analyzed the provenance of the sediments based on conservative chemical elements that can vary as a function of the source material (Retallack, 1997). We used Ti/Zr and Cr/Zr ratios as provenance indices, as they are often used when inert minerals such as quartz are abundant in the sediments (McLennan, 2001; Sheldon and Tabor, 2009; Kassi et al., 2015; Mitchell and Sheldon, 2016). A global database of chemical composition of fluvial sediments, including data from sixty different studies, reports a global average Ti/Zr ratio of 27.5 and Cr/Zr ratio of 0.81 (Viers et al., 2009). McLennan (2001) reports average Cr/Zr values of 0.44

for the upper continental crust, a value that is often used as a reference in other studies (Mitchell and Sheldon, 2016; Viers et al., 2009). An increase of the Cr/Zr ratio points to a higher proportion of mafic rocks relative to felsic ones (McLennan, 2001; Varga et Szakmany, 2004; Kassi et al., 2015).

We analyzed the weathering extent of the sediments based on major and trace element ratios (Table 1). The chemical index of alteration (dimensionless) is a measure of the overall weathering extent (Nesbitt and Young, 1982; Sheldon and Tabor, 2009; Ameijeiras et al., 2017; Vanacker et al., 2019). We then investigated specific weathering processes. We measured hydrolysis with $Al_2O_3/SiO_2$ and Ba/Sr ratios. The $Al_2O_3/SiO_2$ ratio fluctuates between 0.0 and 0.3 in most soils, but can reach values that are higher than 0.3 in very clayey layers (Retallack, 1997). The Ba/Sr ratio is an indicator of leaching, and ranges from 2 in most rocks to 10 in very acidic soils (Retallack, 1997; 2019). An intensively leached paleosoil typically presents lower Ba/Sr values in the top horizons compared to the less weathered deeper horizons (Sheldon and Tabor, 2009). The redox condition is analyzed by the $\frac{Fe_2O_3+MnO}{Al_2O_3}$ ratio (Retallack, 2019; Ivanova et al., 2019), as $Fe_2O_3$ and MnO are released from silicate minerals by hydrolysis and can precipitate as surface coatings or concretions in oxidized sediments (Cornu et al., 2009).

The provenance and weathering indices were plotted as function of depth. For each unit (U1-6), we determined its mean and standard deviation. Additionally, the population of each provenance and weathering index within a unit was compared to the population from the adjacent unit(s) with the Mann-Whitney U test (Table 2). This non-parametric equivalent of the t-test is developed for populations with low ($n < 12$) number of observations (Mann and Whitney, 1947). Significant differences between units were considered at a two-tailed level of confidence (p-value < 0.05).

*Table 1. Geochemical indices for the characterization of provenance and weathering*

| Ratio/index | Formula | Description |
|---|---|---|
| Chemical index of alteration (CIA) | $\frac{Al_2O_3 \text{ x } 100}{K_2O + Na_2O + CaO + Al_2O_3}$ | Indicator of mobility of $Ca^{2+}$, $K^+$ and $Na^+$ with reference to $Al^{3+}$ as result of formation of clay minerals from feldspar weathering. The index increases as weathering extent advances. |
| Clayeyness | $\frac{Al_2O_3}{SiO_2}$ | Indicator of hydrolysis, clay formation and clay mineralogy. |
| Oxidation intensity | $\frac{Fe_2O_3 + MnO}{Al_2O_3}$ | Indicator of redox condition. Higher ratios are indicative of higher oxidation. |
| Ba/Sr | Ba/Sr | Indicator of leaching, determined by ratio of two chemically similar elements of different solubility. The ratio increases with degree of drainage and time of weathering from 2 in most rocks to >10 in strongly leached regolith. |
| Cr/Zr | Cr/Zr | Indicator of sediment provenance, determined by ratio of two conservative elements. Higher Cr/Zr ratios indicate higher contributions from mafic sources comparatively to felsic ones. |
| Ti/Zr | Ti/Zr | Indicator of sediment provenance, determined by ratio of two conservative elements. The Ti and Zr concentrations in sediments vary as a function of the source materials. |

## 4.3 In-situ produced $^{10}$Be concentrations

The $^{10}$Be concentration of a fluvial deposit can accurately be described by Eq. (1), where the concentration of $^{10}$Be atoms in a sample, C(z,t) [at.$g_{qtz}^{-1}$], accumulates as function of depth below the earth surface (z) and time (t). Erosion of the overburden, expressed by E [cm.$yr^{-1}$], reduces the concentration of $^{10}$Be atoms. Sediments can contain an inherited $^{10}$Be concentration ($C_{inh}$) accumulated during previous exposure in the source areas and/or during transport and temporary storage in fluvial systems. The measured $^{10}$Be concentration is the sum of the inherited and the post-depositional $^{10}$Be atoms per mass of quartz:

$$C(z,t) = C_{inh}(z)\, e^{-\lambda t} + \frac{P(z)}{\lambda + \frac{\rho E}{\Lambda}}\, e^{-\frac{\rho (z_0 - E t)}{\Lambda}} \times \left(1 - e^{-\left(\lambda + \frac{\rho E}{\Lambda}\right) t}\right) \qquad (1)$$

The production rate $P(z)$ is described by Eq. (2):

$$P(z) = P(z_0)\, e^{\left(\frac{-z \rho}{\Lambda}\right)} \qquad (2)$$

where $P(z_0)$ [at.$g_{qtz}^{-1}$.$yr^{-1}$] is the production rate at the surface, where the depth, z [cm], equals 0, $\Lambda$ [$g.cm^{-2}$] is the path attenuation length, $\rho$ [$g.cm^{-3}$] is the density of the overburden, $\lambda$ [$yr^{-1}$] is the decay constant of $^{10}Be$.

Sediment samples were processed for in-situ cosmogenic $^{10}Be$ analyses following the procedure described in Vanacker et al. (2015). Samples were washed, dried, and sieved, and the 500–1000 µm grain size fraction was used for further lab processing. Quartz was extracted by magnetic separation and chemical leaching with low concentration of acids (HCl, $HNO_3$, and HF) in an overhead shaker. Purified quartz samples of 20-40 g of quartz were then leached with 24% HF for 1 h to remove meteoric $^{10}Be$, followed by spiking with $^{9}Be$ and total decomposition in concentrated HF. The Beryllium in solution was extracted by ion exchange chromatography as described in von Blanckenburg et al. (1996). Three blanks were processed. About 200 µg of $^{9}Be$ carrier was added to blanks and samples. The $^{10}Be/^{9}Be$ ratios were measured using accelerator mass spectrometry on the 500 kV Tandy facility at ETH Zürich (Christl et al., 2013). The $^{10}Be/^{9}Be$ ratios were normalized with the in-house standard S2007N and corrected with the average $^{10}Be/^{9}Be$ ratio of three blanks of $1.3 \pm 0.6 \times 10^{-14}$. The analytical uncertainties on the $^{10}Be/^{9}Be$ ratios of blanks and samples were then propagated into the one standard deviation analytical uncertainty for $^{10}Be$ concentrations. We then plotted the $^{10}Be$ concentrations and their respective uncertainties as function of depth below the surface.



4.5 Analyses of co-variation

Co-variation between granulometry, geochemical indices of sediment provenance and weathering extent, and in-situ $^{10}Be$ concentration, was studied based on Spearman correlation analyses (Table 3). As the sampling scheme for the in-situ $^{10}Be$ analyses slightly differs from the one for geochemical characterization, we matched the in-situ $^{10}Be$ data with the geochemical data of the sample(s) of the corresponding unit.

## 5. Results

### 5.1 Field observations

Based on granulometry and sorting, presence of coatings and concretions, and sedimentary structures, we identified six units (U1-6) in the As profile that are separated from each other by sharp contacts (Fig. 3): The lowermost unit (U1) extends between 700 and 547 cm depth, and is characterized by flat and low-angle cross laminations of poorly sorted material. In the gravel facies classification of Miall (1996), it corresponds to a crudely bedded gravel bedform (Gh) that ranges from gravels cemented in a sandy matrix to > 10 cm large pebbles (Fig. 3e and f). Gravels and coarser sediments are sub-angular to sub-rounded, and often imbricated. Below 6.50 m, the exposure is dark orange because of iron oxide coatings. The color of the gravel coatings changes to dark black between 560 and 547 cm depth. The second unit (U2), between 547 and 520 cm has an inclined contact of low angle (<10°) with the underlying unit, U1. It appears as a light-colored layer of loamy sand (Fig. 3c), that does not present any particular sedimentary structure and was therefore classified as massive sand (Sm). The third unit (U3) is then observable between 520 and 335 cm depth and presents a horizontally stratified gravel facies (Gh) with some imbrications. It is constituted of fine to very coarse gravels with sub-angular to sub-rounded shapes, in a sandy matrix with orange-brownish coating (Fig. 3c and g). The following unit (U4, between 335 and 235 cm) has similar granulometry as U3 but different color, i.e., light brown. The sedimentary structure shows planar lamination and no imbrications were observed. Then, in the fifth unit (U5, between 235 and 140 cm), the fluvial deposits are arranged in mostly flat laminations with a majority of coarse sand (Sh) and some fine and medium-sized gravels. Finally, the uppermost unit (U6, between 140 and 60 cm) corresponds to a loamy sand (Sh) in which gravels become very scarce (Fig. 3d). The unit U6 presents an irregular contact at the top (Fig. 3) with a homogeneous sand package that is interpreted as the Weichselian cover sand (Beerten et al., 2017).

5.2. Depth variation in provenance and weathering

Provenance of sediments, as measured by Ti/Zr and Cr/Zr, varies considerably within the deposits (Fig. 4): Ti/Zr values range between 4 and 15, and Cr/Zr values between 0.12 and 0.56. The two indices are significantly correlated (r = 0.81, p-value < 0.01; Table 3) and show a very similar pattern with depth. The Mann-Whitney test shows significant differences of Cr/Zr and Ti/Zr values between U5 and U4, and U4 and U3. With the exception of units U4 and U5 that show little (< 15%) variation in provenance, all other units (U1, U3 and U6) show considerable variation in Ti/Zr and Cr/Zr within the unit. Remarkably low values are reported for the bottom part of U6.

Weathering extent, as measured by the CIA, fluctuates between 70 and 88, and exhibits significant differences between U5 and U4 and marginally significant differences between U4 and U3. The CIA is correlated to grain size (r=0.80, p-value < 0.01), to the oxidation index $\frac{Fe_2O_3+MnO}{Al_2O_3}$ (r = 0.47, p-value < 0.1), $Fe_2O_3$ (r = 0.60, p-value < 0.05), and Ba/Sr (r = 0.61, p-value < 0.01). The Ba/Sr ratio fluctuates between 10 and 26, except in the bottom of U6 where it reaches a value of 52. As for provenance indices, Ba/Sr values are significantly different between U5 and U4 and between U4 and U3 (Table 2). The variation within the U1, U3 and U6 units is larger than the variation between the units. The Ba/Sr is positively correlated to MnO (r = 0.58, p-value < 0.05), oxidation index $\frac{Fe_2O_3+MnO}{Al_2O_3}$ (r = 0.72, p-value < 0.01), and is negatively correlated to $K_2O$ (r = -0.86, p-value < 0.01). Among all alkali and alkaline earth elements, only the concentration of $K_2O$ is represented in Fig. 4, as similar trends are observed for the other elements which are less abundant. The $K_2O$ concentration decreases from 2.5% to less than 1% in U6. The Mann-Whitney test reveals that it is significantly lower in the U3 in comparison to the U4 and does not show a specific trend in the other units (Table 2).

The $Al_2O_3/SiO_2$ ratio is significantly different between all units except for U6 and U5. The $Al_2O_3/SiO_2$ is correlated with Cr/Zr (r = 0.56, p-value < 0.05), Ti/Zr (r = 0.79, p-value < 0.01), $K_2O$ (r = 0.66, p-value < 0.01) and $Fe_2O_3$ (r = 0.46, p-value < 0.1). The concentration in iron oxides ($Fe_2O_3$) fluctuates in all units between 2 and 4%. In U3, it is significantly more abundant than in U4, and marginally more abundant than in U1 and U2. Manganese oxide (MnO) concentrations vary by several orders of magnitude within the profile. The three uppermost units do not show much variability in MnO with values close to 0.01%. In the lower units of U1 and U3, the MnO concentration is significantly higher than in the overlying units (Table 2) with mean MnO concentrations of respectively 0.42 and 1.11%. Within U1, values up to 2.70% of MnO are reported (Fig. 4). The oxidation index $\frac{Fe_2O_3+MnO}{Al_2O_3}$ follows the same pattern as MnO, but reports stronger differences between U6 and U5. As expected, the three latter indices ($Al_2O_3/SiO_2$, MnO and $\frac{Fe_2O_3+MnO}{Al_2O_3}$) are strongly correlated (Table 3).

*Table 2. Analyses of differences in provenance and weathering extent between the units (U1-U6). The significance of the differences was tested with a Mann-Whitney test with level of confidence of 95%.*

| | | Ti/Zr | Cr/Zr | Ba/Sr | $\frac{Al_2O_3}{SiO_2}$ | $\frac{Fe_2O_3+MnO}{Al_2O_3}$ | MnO | $Fe_2O_3$ | $K_2O$ |
|---|---|---|---|---|---|---|---|---|---|
| ***U6-U5*** | Statistic | 3 | 3 | 3 | 3 | 1 | 1 | 2 | 3 |
| | P-value | 0.33 | 0.33 | 0.33 | 0.33 | 0.01 | 0.1 | 0.19 | 0.33 |
| ***U5-U4*** | Statistic | 0 | 0 | 0 | 1 | 0 | 0 | 4 | 1 |
| | P-value | 0.04 | 0.04 | 0.04 | 0.01 | 0.04 | 0.04 | 0.5 | 0.09 |
| ***U4-U3*** | Statistic | 1 | 0 | 0 | 0 | 0 | 0 | 0 | 0 |
| | P-value | 0.01 | 0.04 | 0.04 | 0.04 | 0.04 | 0.04 | 0.04 | 0.04 |
| ***U3-U1*** | Statistic | 2 | 3 | 4 | 0 | 3 | 3 | 2 | 1 |
| | P-value | 0.11 | 0.18 | 0.3 | 0.03 | 0.18 | 0.18 | 0.11 | 0.06 |
| ***U3-U1/U2*** | Statistic | 3 | 3 | 4 | 0 | 6 | 3 | 2 | 3 |
| | P-value | 0.12 | 0.12 | 0.18 | 0.02 | 0.38 | 0.12 | 0.06 | 0.12 |

5.3. Depth variation in grain size

The samples of the Zutendaal deposits span a wide range of grain sizes (Fig. 4). The lowest unit, U1, shows a bimodal grain size distribution with a medium gravel and medium to coarse sand component. On average, more than 70% of U1 is composed of gravel. The grain size distribution is homogeneous within the U1 unit showing no systematic trend with depth. The U2 unit has a distinct granulometry with a unimodal grain size distribution with 90% of its weight pertaining to the sand fraction. A fining upward trend from U1 to U2 is thus identified by the D50. Within U2, two separate sub-layers can be identified: the lowest part of U2, composed of coarse sands, is capped by an upper layer of about 10 cm composed of fine sands.

Compared to U2, the unit U3 has a dominant (≥ 80%) gravel component. By its unimodal distribution with central mode in the medium gravels, it is distinct from U1 and U2. A transition exists between the top of U3 and bottom part of U4, with a gradual increase in the sand component in U4. This corresponds to a slight decrease of the D50. The bimodal distribution of U4 is comparable to U1 with a mode in the medium gravel and medium to coarse sand fraction. At the top of U4, a 10 cm thick layer of fine sands is present, similar to what we observed at the top of U2. In contrast to U1, U3 and U4, the unit U5 has a predominantly (80%) sand fraction with the percentage of sand increasing at the top of the unit, so that the D50 shows a fining upward trend from U4 to U5. The uppermost unit, U6, has a unimodal grain size distribution with a mode in the medium to fine sand fraction, which makes it contrastively finer compared to the U5.

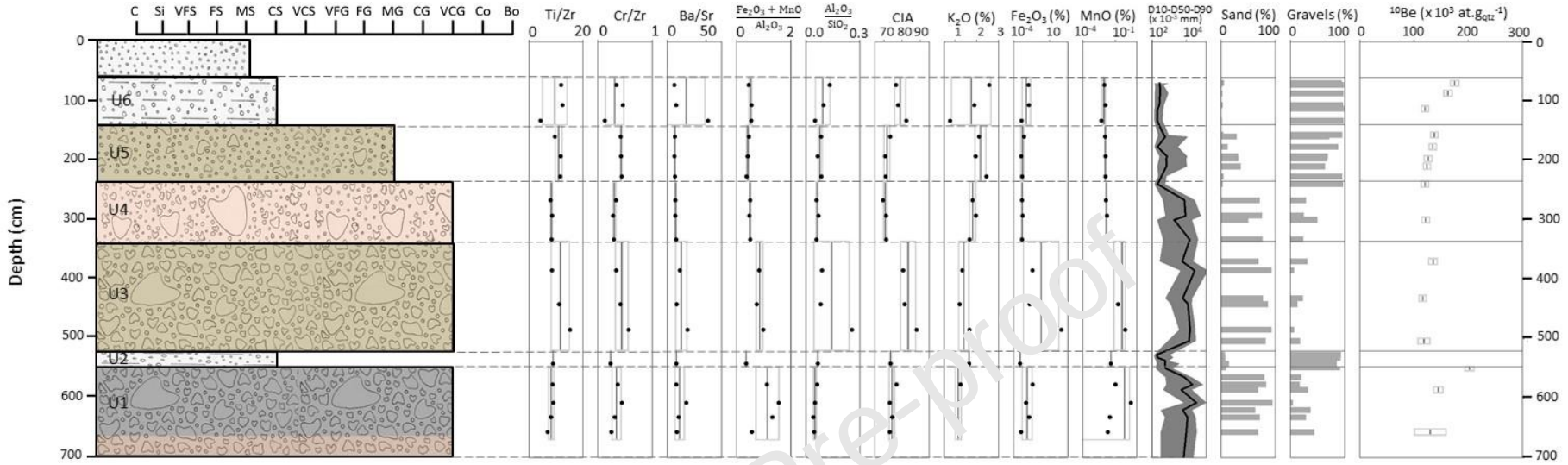


*Fig. 4. Plot of field observations,provenance and weathering indices, granulometry and $^{10}$Be concentrations as function of depth. For the geochemical indices, the results are plotted for the individual samples as dots. The boxes represent the mean (black line) and standard deviation (grey line) of the measurements per unit (U1-6). The MnO oxide data are plotted with a logarithmic x-axis. The granulometry is represented by the D50 (black line), and the grey area delimits the D10 (left) and the D90 (right). The gravel (> 2mm) and sand (<2 mm) fractions are presented as horizontal stacked bar plots. The in-situ $^{10}$Be concentrations (mean ± 1 standard deviation) are plotted per sample, whereby the height of the box represents the thickness of the sampling interval.*

*Table 3. Spearman correlation between grain size (fraction below 0.25 mm), geochemical indices of provenance and weathering, and $^{10}$Be concentration.*

** p-value < 0.10, ** p-value <0.05 and *** p-value < 0.01.*

| | **Grain size** | **CIA** | **Ti/Zr** | **Cr/Zr** | **Ba/Sr** | $\frac{Al_2O_3}{SiO_2}$ | $\frac{Fe_2O_3 + MnO}{Al_2O_3}$ | **MnO** | **$Fe_2O_3$** | **$K_2O$** |
|---|---|---|---|---|---|---|---|---|---|---|
| **CIA** | 0.80*** | | | | | | | | | |
| **Ti/Zr** | 0.21 | 0.16 | | | | | | | | |
| **Cr/Zr** | 0.05 | 0.08 | 0.81*** | | | | | | | |

| | | | | | | | | | | |
|---|---|---|---|---|---|---|---|---|---|---|
| **Ba/Sr** | 0.40 | 0.61*** | -0.33 | -0.14 | | | | | | |
| $\frac{Al_2O_3}{SiO_2}$ | 0.37 | 0.32 | 0.79*** | 0.56** | -0.29 | | | | | |
| $\frac{Fe_2O_3 + MnO}{Al_2O_3}$ | 0.14 | 0.47* | -0.19 | 0.19 | 0.72*** | -0.27 | | | | |
| **MnO** | -0.12 | 0.21 | 0.00 | 0.16 | 0.58** | -0.06 | 0.63*** | | | |
| **$Fe_2O_3$** | 0.24 | 0.60** | 0.38 | 0.54** | 0.26 | 0.46* | 0.65*** | 0.44* | | |
| **$K_2O$** | -0.20 | -0.42* | 0.58** | 0.36 | -0.86*** | 0.66*** | -0.70*** | -0.43* | 0.06 | |
| **$^{10}$Be conc.** | 0.14 | -0.08 | -0.19 | -0.60** | -0.37 | -0.12 | -0.24 | -0.30 | -0.21 | 0.19 |

5.4. Depth variation in in-situ produced $^{10}$Be concentrations

The in-situ $^{10}$Be concentrations vary from 120 x $10^3$ to more than 200 x $10^3$ at.$g_{qtz}^{-1}$ (Table 4). Most of the uncertainties are in the range of 5 to 7% of the measured $^{10}$Be concentrations. The observed CRN depth variation deviates from a simple exponential decrease of $^{10}$Be concentration with depth, and points to a complex deposition history. The upper three values (70 to 113 cm, corresponding to U6) show a steady decrease from 180 x $10^3$ to 120 x $10^3$ at.$g_{qtz}^{-1}$ (Fig. 4). We observed an abrupt change in the concentration at 157 cm depth, corresponding to 137 x $10^3$ at.$g_{qtz}^{-1}$ measured at the top of the U5 unit. The following five samples present a slight decrease of concentration with depth throughout the U5 and U4 units. Similar as we observed at the top of U5, the upper sample of the U3 unit has a $^{10}$Be concentration of 135 x $10^3$ at.$g_{qtz}^{-1}$ at 370 cm depth, about 12% higher than the sample taken at 300 cm depth. The following two samples in U3 show a steady decrease in $^{10}$Be concentration with depth. At the bottom of the profile, in the upper part of U1, a third local maximum of $^{10}$Be concentration is found. The value of 202 x $10^3$ at.$g_{qtz}^{-1}$ measured at 550 cm depth is the highest value that was measured in the profile and is 50% higher than the average $^{10}$Be concentration measured in the overlying units. The samples taken in U1 show a steady decrease of $^{10}$Be concentration with depth, from 145 x $10^3$ at.$g_{qtz}^{-1}$ at 586 cm to 130 x $10^3$ at.$g_{qtz}^{-1}$ at 657 cm depth.

*Table 4. Analytical results of the in-situ produced $^{10}$Be concentration.*

| Sample label | Unit | Field code | Depth (cm) | Quartz (g) | $^{9}$Be carrier (mg) | $^{10}$Be/ $^{9}$Be (x $10^{-12}$) | $^{10}$Be (x $10^{3}$ at.$g_{qtz}^{-1}$) |
|---|---|---|---|---|---|---|---|
| TB3824 | U6 | Heras-18 | 70 | 38.074 | 0.266 | 0.387 ± 0.015 | 175.0 ± 7.8 |
| TB3823 | U6 | Heras-17 | 87 | 38.716 | 0.220 | 0.443 ± 0.018 | 162.8 ± 7.6 |
| TB3822 | U6 | Heras-16 | 113 | 38.957 | 0.267 | 0.275 ± 0.013 | 120.7 ± 6.7 |
| TB3820 | U5 | Heras-14 | 157 | 38.123 | 0.264 | 0.309 ± 0.012 | 137.6 ± 6.7 |
| TB3819 | U5 | Heras-13 | 177 | 37.097 | 0.220 | 0.355 ± 0.014 | 134.9 ± 6.7 |
| TB3818 | U5 | Heras-12 | 197 | 37.774 | 0.266 | 0.280 ± 0.014 | 126.2 ± 7.3 |
| TB3821 | U5 | Heras-15 | 210 | 38.204 | 0.266 | 0.278 ± 0.012 | 123.8 ± 6.6 |
| TB3817 | U4 | Heras-11 | 240 | 38.046 | 0.266 | 0.270 ± 0.013 | 120.4 ± 7.0 |
| TB3816 | U4 | Heras-10 | 300 | 37.874 | 0.220 | 0.327 ± 0.016 | 121.6 ± 7.1 |

| | | | | | | | |
|---|---|---|---|---|---|---|---|
| TB3815 | U3 | Heras-09 | 370 | 37.399 | 0.267 | 0.295 ± 0.015 | 135.3 ± 8.0 |
| TB3814 | U3 | Heras-08 | 432 | 37.850 | 0.268 | 0.258 ± 0.012 | 116.5 ± 6.6 |
| TB3813 | U3 | Heras-07 | 504 | 21.156 | 0.268 | 0.152 ± 0.011 | 118.4 ± 10.9 |
| TB3812 | U1 | Heras-06 | 550 | 37.437 | 0.268 | 0.435 ± 0.015 | 202.5 ± 8.3 |
| TB3811 | U1 | Heras-04 | 586 | 33.597 | 0.268 | 0.284 ± 0.014 | 145.1 ± 8.5 |
| TB4346 | U1 | Heras-02 | 657 | 10.265 | 0.296 | 0.078 ± 0.014 | 130.0 ± 29.7 |
| TB3829 | | n/a | n/a | 0.000 | 0.220 | 0.006 ± 0.002 | |
| TB3830 | | n/a | n/a | 0.000 | 0.267 | 0.018 ± 0.005 | |
| TB4349 | | n/a | n/a | 0.000 | 0.219 | 0.015 ± 0.004 | |

## 6. Discussion

### 6.1 Identification of sedimentary units

Based on grain size, three fining upward cycles can be distinguished in the gravel deposits (Fig. 4). A first fining upward sequence (700 to 520 cm depth) contains U1 and U2: the gravel dominated sediments of U1 become abruptly finer in U2 where we observe a transition from coarse to fine sands. It is likely that U2 represents an infill of a shallow, abandoned channel and covers earlier active channel bar deposits from U1. A second fining upward sequence (520 to 235 cm depth) shows another, less abrupt, transition from medium gravels to medium and fine sands. This sequence, which incorporates U3 and U4, can be indicative of shallowing of the riverbed, and probably corresponds to a gravel bar top that is mantled with sand when stream discharge and competence diminish (Collinson, 1996). Finally, a third sequence (235 to 70 cm) is observed in U5 and U6, with a shift from a bimodal gravel and sand distribution in U5 to a predominantly fine sand in U6.

Looking at provenance variability, Cr/Zr values of all samples are close to the reference value of 0.44 found in the upper continental crust (McLennan, 2001). The absolute variability of Cr/Zr ratios in the Zutendaal gravels is low compared to global variation in Cr/Zr ratios reported by Viers et al. (2009). Similarly, the Ti/Zr ratios show little absolute variation, and are about two to three times lower than the global average (McLennan, 2001; Viers et al., 2009). The relatively low variation in provenance with respect to global databases can

indicate that the deposits originate from the same source areas. Within the profile, only the U4 unit shows different provenance values, with distinctly lower values than U5 and U3 (Table 2).

With regard to weathering extent, we found a succession of four weathering zones that display different weathering types and extents. Chemical weathering by hydrolysis is weak throughout the profile as shown by $Al_2O_3/SiO_2$ ratios that never exceed 0.3 within the Zutendaal gravels. The Ba/Sr ratios show deviating results with values exceeding the critical value of 9 that is associated by intense hydrolysis by Retallack (2019). However, the exact values of the Ba/Sr ratios are uncertain given that Sr concentrations in the samples were close to the detection limit. When reading the profile from bottom to top, the U1 and U2 units show high oxidation and low hydrolysis. The $Al_2O_3/SiO_2$ ratios are consistently low compared to the overlying unit U3, and the CIA and $K_2O$ show evidence of low base cation leaching. The three uppermost samples of U1 are intensively oxidized based on $\frac{Fe_2O_3+MnO}{Al_2O_3}$ index. A second weathering zone corresponds to the U3 unit and is characterized by the most advanced weathering extent of the profile. Both CIA and $K_2O$ show evidence of advanced base cation leaching. In U3, we observe higher-than-average concentrations of MnO and $Fe_2O_3$ and $Al_2O_3/SiO_2$, and the $\frac{Fe_2O_3+MnO}{Al_2O_3}$ index. A third zone corresponds to U4 and U5. Although chemically distinct from each other based on the Mann Whitney test (Table 2), they appear similar when they are compared to the other units of the profile as they have the lowest extent of chemical weathering of the profile. A low base cation leaching and a low oxidation level are concomitantly present in the U4 and U5. Finally, the U6 can be considered as a separate fourth weathering zone, with base cation leaching and oxidation higher than in the U5.

Based on the cosmogenic radionuclide analysis, we identified four $^{10}$Be concentration maxima, that are located in the upper part of U1, U3, U5 and U6. A positive deviation in the $^{10}$Be concentration-depth profile is indicative for a stable period that lasted several kyr so that $^{10}$Be nuclides accumulated at the top of the unit. It also implies that eventual erosional events did not remove (entirely) the previously deposited material. Such pattern is particularly well developed in the U1 unit, with (i) strong decrease of the $^{10}$Be concentration with depth and (ii) significantly higher concentrations in the two upper samples, TB 3811 and TB 3812, compared to the samples in the overlaying unit, U3. This local $^{10}$Be concentration maximum likely represents the longest hiatus in sedimentation. Similar observations were made for U3 and U5, although the local deviation in $^{10}$Be is less pronounced.

6.2 Co-variation between grain size, elemental geochemistry and $^{10}$Be concentration

Based on co-variations between grain size, provenance and weathering indices, and in-situ produced $^{10}$Be concentration, we can reconstruct the depositional history of Zutendaal gravels. The correlation between $Al_2O_3/SiO_2$ and provenance indicates that the weak extent of hydrolysis throughout the entire profile is more related to pre-depositional weathering than to intraformational or post-depositional weathering. In contrast, the MnO and $\frac{Fe_2O_3+MnO}{Al_2O_3}$ index (Table 3) are not significantly related to provenance, which indicates that the deposits have been weathered by oxidation after their final deposition. Moreover, as $\frac{Fe_2O_3+MnO}{Al_2O_3}$ and MnO are highest in U1 and U3 that contain individual decreasing exponential $^{10}$Be concentrations with depth, the two lower oxidation zones likely developed during hiatuses between aggradation phases. Weathering by oxidation can be intraformational. However, we cannot exclude that the iron and manganese coatings developed later on, after the Meuse River shifted its course eastward (Fig. 2) and started to incise in its own deposits. Chemical weathering during this period can have overprinted earlier weathering signals.

The absence of a systematic co-variation between provenance and in-situ produced $^{10}$Be concentrations is indicative of changes in the aggradation mode that are not associated with changes in sedimentary provenance. This is particularly clear in the three lowermost units (U1, U2 and U3) where the two exponentially decreasing $^{10}$Be concentration-depth profiles (at the top of U1 and U3) are not associated with changes in Cr/Zr and Ti/Zr ratios. This observation affirms the existence of two long hiatuses, marked as H1 and H2 in Fig. 5, in the sedimentary sequence during which the provenance of sediments remained unchanged. On the other hand, aberrant provenance values for individual samples can be indicative of uncommon sample sources, and be associated to particular sample sourcing, deposition or erosion events. This can be the case for the sample taken at 133 cm depth in U6, for which provenance indices are strongly different from the two overlying (U6) and three underlying (U5) geochemical datapoints (Fig. 4). The adjacent $^{10}$Be sample of the same unit, U6, also shows a lower-than-expected $^{10}$Be concentration when fitting Eq. (1) through the $^{10}$Be data of the unit (Fig. 5). Further analyses are needed to study the potential effect of aberrant provenance on in-situ $^{10}$Be values, whereby paired samples are analyzed for CRN, provenance and weathering.

The absence of a correlation between grain size and provenance shows that grain size is not related to the source of the sediments (Table 3). This is also exemplified by the observation at the limit between U3 and U4 where a change in provenance is not associated with a change in grain size (Fig. 4). Similar observations were made for grain size and weathering indices where, except for CIA, no correlation is found (Table 3).

6.3. Relating co-variation information to the depositional history of fluvial sediments.

Co-variations between grain size, provenance and weathering, and in-situ $^{10}$Be concentrations can enhance our understanding of the (post-)depositional history of fluvial

deposits. Here, we applied the conceptual framework (Fig. 1) to the exposure of the Zutendaal gravels (Fig. 5). First, we explored the aggradation mode of the deposits. Fining upward sequences witness individual aggradation phases, while in-situ CRN concentration-depth profiles can provide information on the duration of the interruptions of deposition during which CRN accumulated at the top of the fining upward sequence. Therefore, combining grain size and CRN data allows one to grasp the history of the sedimentary sequences. When the upper limit of fining upward sequences does not coincide with a local maximum in the CRN concentration-depth profile, i.e., the U4-U5 boundary in the Zutendaal gravels, then the hiatus (indicated by H3 in Fig. 5) can be as short as a few days (Miall, 1996). Conversely, when a CRN maximum is observed at the top of a fining upward sequence, the surface was exposed for a prolonged period of time and the length of the hiatus can be estimated from the $^{10}$Be concentration-depth profile. In the study site, a long hiatus is observed at the top of U1. When assuming that the sediments in U1 and U3 have equal inheritance and were subject to a negligible amount of denudation and post-burial $^{10}$Be production, we can estimate a minimum duration of exposure of the U1 surface of about 19 kyr. Erosion of U1 or U2 after deposition, or slow aggradation of U2, would result in a longer hiatus' duration, even up to a glacial cycle. The analysis of presence and absence of co-variations between CRN and granulometry can therefore contribute to decipher fluvial dynamics over the Pleistocene.

Second, if the pre-depositional history of sediments differs, they can have a different inherited CRN concentration. Such differences can produce local anomalies in the CRN concentration-depth profiles. Co-variation of such CRN anomalies with provenance proxies can provide insights in different origin, exposure history or transport time of the sediment (Fig. 6). Besides, by analyzing correspondence between CRN concentration and provenance, it is possible to identify aberrant samples where the CRN concentration deviates from the expected one because of differences in nuclide inheritance. In such a case, the inheritance can be used as a measure of the pre-depositional history and denudation rate in

the source area (e.g., Schaller et al., 2001). The third uppermost sample (taken at 133 cm depth in U6, Fig. 4) shows evidence of unusual inheritance, and might have an effect on the $^{10}$Be concentration determined for the lower part of U6.

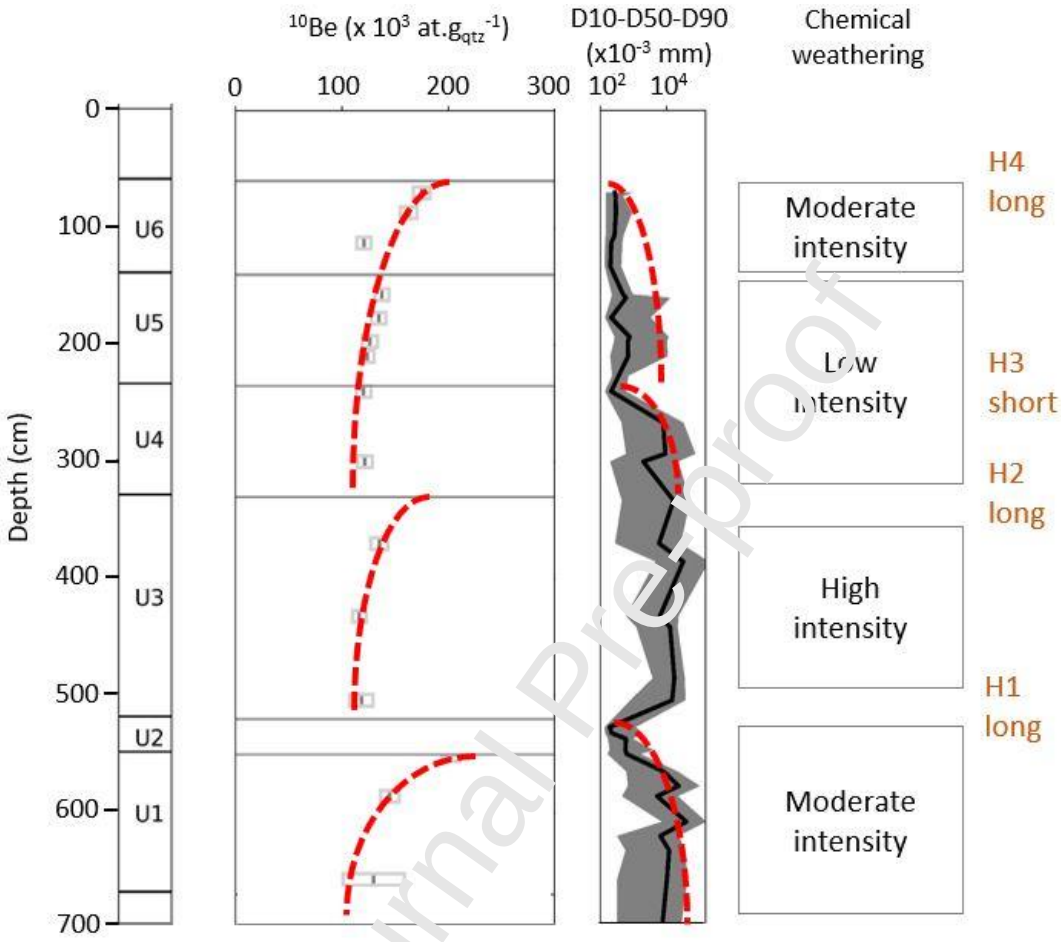


*Fig. 5. Conceptual summary of co-variation between in-situ $^{10}$Be concentrations, grain size, and weathering extent in the outcrop of fluvial deposits. When a local maximum of CRN concentration coincides with the top of a fining upward sequence (like H1 between U1-U2 and U3, and H4 between U6 and the Weichselian sands from the Gent Formation), there is evidence for a hiatus that lasted at least several thousands of years. Conversely, short hiatuses will not leave any particular imprint in the $^{10}$Be concentration, as shown in case H3. The same is true for the chemical weathering extent that shows little variation over short hiatuses (like in U4-U5).*

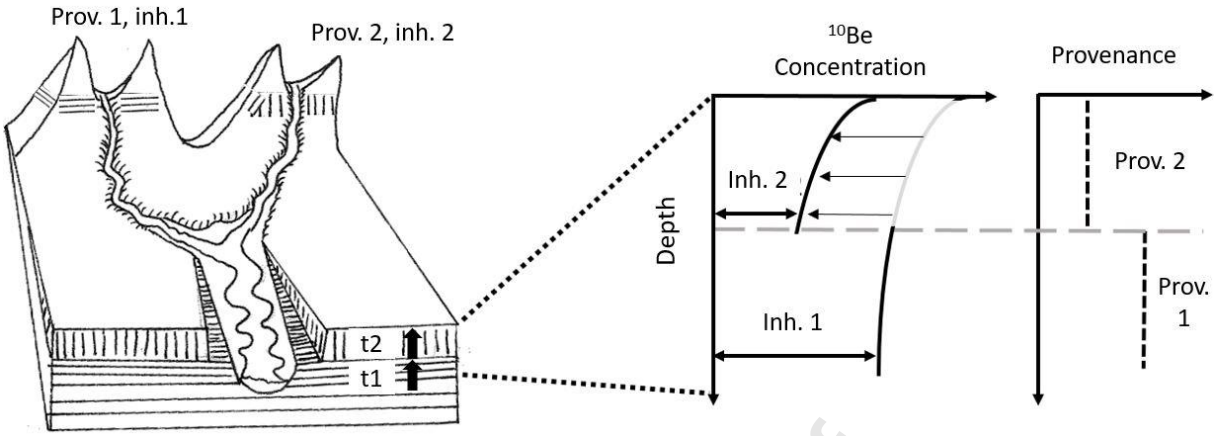


*Fig. 6. Sketch showing how differences in exposure to cosmic rays in the source areas can affect the CRN concentration-depth profiles in a sedimentary sink. Two sub-catchments with different provenance (Prov.1 and Prov.2) and erosion rate supply sediments to the river system. During a first phase of aggradation; t1, sediments are mainly supplied from Prov.1 sources and stored in a sedimentary sink. Then, during a second phase, t2, most of the sediments are supplied from the Prov.2 source area. Given that erosion rates are lower in Prov.1 compared to Prov.2, the sediments were longer exposed to cosmic rays and have higher CRN concentrations. Such a difference in exposure in the source area can be propagated into the inherited $^{10}$Be concentration (Inh.1 and Inh.2) of fluvial sediments.*

Finally, in climate-controlled river terrace formation, the absence of deposition rather occurs during warm-cold and cold-warm transitions (Vandenberghe, 2015), although periglacial conditions may also induce hiatuses in the deposition process during cold phases. Intraformational weathering patterns that co-vary with CRN concentration-depth profiles can inform us on the past environmental conditions that prevailed during the corresponding hiatus. Such a co-variation (as observed in U1-U2, Fig. 5) generates additional information on the climate during the transition periods, as it differentiates them from hiatuses that would occur over colder phases during which weathering was essentially inhibited in northwestern Europe.

## 7. Conclusion

We explored co-variations between grain size, geochemical indices of weathering and provenance and in-situ $^{10}$Be concentrations to assess how they can generate complementary information on the source, depositional mode and deposition history of braided river deposits. We developed a conceptual framework that was applied to the Zutendaal gravels, a

Pleistocene fluvial deposit in northeastern Belgium. Data were acquired from bulk samples collected in the geosite Hermans, in the municipality of As. Based on grain size, provenance and weathering indices, and in-situ $^{10}$Be concentrations, we defined sedimentary units with distinct depositional history. The case study demonstrated how an integrated analysis can provide new insights on the fluvial dynamics and landscape stability during the Pleistocene. The main findings are (1) co-variation between grain size and $^{10}$Be concentration can be used to constrain the duration of hiatuses in sedimentary records, (2) anomalies in $^{10}$Be concentration caused by inheritance can be flagged based on provenance analysis, and (3) co-variation between chemical weathering extent and $^{10}$Be concentration can inform us on the environmental conditions during hiatuses. The conceptual framework can be applied to fluvial sediments to study climate-controlled fluvial system change and incision during the Pleistocene.

**Acknowledgements**

NV acknowledges funding from a teaching assistantship from the Faculty of Sciences, UCLouvain, and FC from the Fonds National de Recherche Scientifique (FRS-FNRS, Belgium). This work was undertaken in close cooperation with, and with the financial support of, NIRAS/ONDRAF, the Belgian Agency for Radioactive Waste and Fissile Materials, as part of the programme on geological disposal of high-level/long-life radioactive waste that is carried out by NIRAS/ONDRAF. The authors thank Marco Bravin for assistance with manipulation and processing samples in the ELIc laboratory.

**References**

Akçar, N., Ivy-Ochs, S., Alfimov, V., Schlunegger, F., Claude, A., Reber, R., Christl, M., Vockenhuber, C., Dehnert, A., Rahn, M., Schlüchter, C., 2017. Isochron-burial dating of glaciofluvial deposits: First results from the Swiss Alps. Earth Surface Processes and Landforms 42, 2414–2425. https://doi.org/10.1002/esp.4201

Ameijeiras-Mariño, Y., Opfergelt, S., Schoonejans, J., Vanacker, V., Sonnet, P., de Jong, J., Delmelle, P., 2017. Impact of low denudation rates on soil chemical weathering intensity: A multiproxy approach. Chemical Geology 456, 72–84. https://doi.org/10.1016/j.chemgeo.2017.03.007

Bartz, M., Rixhon, G., Kehl, M., el Ouahabi, M., Klasen, N., Brill, D., Weniger, G.C., Mikdad, A., Brückner, H., 2017. Unravelling fluvial deposition and pedogenesis in ephemeral stream

deposits in the vicinity of the prehistoric rock shelter of Ifri n'Ammar (NE Morocco) during the last 100 ka. Catena 152, 115–134. https://doi.org/10.1016/j.catena.2016.12.007

Beerten, K., De Craen, M., Wouters, L., 2013. Patterns and estimates of post-Rupelian burial and erosion in the Campine area, north-eastern Belgium. Physics and Chemistry of the Earth 64, 12-20. http://dx.doi.org/10.1016/j.pce.2013.04.003

Beerten, K., Heyvaert, V.M.A., Vandenberghe, D., Van Nieuland, J., Bogemans, F., 2017. Revising the Gent Formation: a new lithostratigraphy for Quaternary wind-dominated sand deposits in Belgium. Geologica Belgica 20(1/2), 95-102. http://dx.doi.org/10.20341/gb.2017.006

Beerten, K., Dreesen, R., Janssen, J., Van Uyten, D., 2018. The Campine Plateau, in: Demoulin, A. (Ed.), Landscapes and Landforms of Belgium and Luxembourg. Springer, Berlin, Germany, pp. 193-214.

Beerten, K., Verbeeck, K., Laloy, E., Vanacker, V., Vandenberghe, D., Christl, M., De Grave, J., Wouters, L., 2020. Electron spin resonance (ESR), optically stimulated luminescence (OSL) and terrestrial cosmogenic radionuclide (TCN) dating of quartz from a Plio-Pleistocene sandy formation in the Campine area, NE Belgium. Quaternary International, 556, 144-158. https://doi.org/10.1016/j.quaint.2020.06.011

Blott, S.J., Pye, K., 2001. Gradistat: A grain size distribution and statistics package for the analysis of unconsolidated sediments. Earth Surface Processes and Landforms 26, 1237–1248. https://doi.org/10.1002/esp.261

Braucher, R., del Castillo, P., Siame, L., Hidy, A.J., Bourlés, D.L., 2009. Determination of both exposure time and denudation rate from an in situ-produced $^{10}$Be depth profile: A mathematical proof of uniqueness. Model sensitivity and applications to natural cases. Quaternary Geochronology 4, 56–67. https://doi.org/10.1016/j.quageo.2008.06.001

Chao, T.T., Sanzolone, R.F., 1992. Decomposition techniques. Journal of Geochemical Exploration 44, 65-106. https://doi.org/10.1016/0375-6742(92)90048-D

Christl, M., Vockenhuber, C., Kubik, P. W., Wacker, L., Lachner, J., Alfimov, V., Synal, H. A., 2013. The ETH Zurich AMS facilities. Performance parameters and reference materials. Nuclear Instruments and Methods in Physics Research Section B: Beam Interactions with Materials and Atoms 294, 29–38. https://doi.org/10.1016/J.NIMB.2012.03.004

Claude, A., Akçar, N., Ivy-Ochs, S., Schlunegger, F., Rentzel, P., Pümpin, C., Tikhomirov, D., Kubik, P.W., Vockenhuber, C., Dehnert, A., Rahn, M., Schlüchter, C., 2017. Chronology of Quaternary terrace deposits at the locality Hohle Gasse (Pratteln, NW Switzerland). Swiss Journal of Geosciences 110, 793–809. https://doi.org/10.1007/s00015-017-0278-z

Cohen K.M., Gibbard, P., 2011. Global chronostratigraphical correlation table for the last 2.7 million years. Subcommission on Quaternary Stratigraphy (International Commission on Stratigraphy), Cambridge, United Kingdom.

Collinson, J.D., 1996. Alluvial Sediments. in: Reading, H.G. (Ed.), Sedimentary Environments: Processes, Facies and Stratigraphy, 3rd Edition. Blackwell Science, Oxford, United Kingdom. pp. 37-81. https://doi.org/10.2307/3514634

Cornu, S., Montagne, D., Vasconcelos, P.M., 2009. Dating constituent formation in soils to determine rates of soil processes: A review. Geoderma 153, 293-303. https://doi.org/10.1016/j.geoderma.2009.08.006

Dreesen, R., Mareels, J., Fries, S., 2005. De zandgroeve van Opgrimbie: een uitzonderlijk kijkvenster op de geologische geschiedenis van de Hoge Kempen. LIKONA Jaarboek 2005, 14–25.

Dehnert, A., Kracht, O., Preusser, F., Akçar, N., Kemna, H. A., Kubik, P. W., Schlüchter, C., 2011. Cosmogenic isotope burial dating of fluvial sediments from the Lower Rhine Embayment, Germany. Quaternary Geochronology 6(3–4), 313–325. https://doi.org/10.1016/j.quageo.2011.03.005

Erlanger, E.D., Granger, D.E., Gibbon, R.J., 2012. Rock uplift rates in South Africa from isochron burial dating of fluvial and marine terraces. Geology 40, 1019–1022. https://doi.org/10.1130/G33172.1

Faust, D., Wolf, D., 2017. Interpreting drivers of change in fluvial archives of the Western Mediterranean - A critical view. Earth-Science Reviews 174, 53-83. https://doi.org/10.1016/j.earscirev.2017.09.011

Gosse, J.C., Phillips, F.M., 2001. Terrestrial in situ cosmogenic nuclides: theory and application. Quaternary Science Reviews 20, 1475-1560. https://doi.org/10.1016/S0277-3791(00)00171-2

Granger, D.E., Muzikar, P.F., 2001. Dating sediment burial with in situ-produced cosmogenic nuclides: theory, techniques, and limitations. Earth and Planetary Science letters 188, 269-281. https://doi.org/10.1016/S0012-821X(01)00309-0

Gullentops, F., Bogemans, F., de Moor, G., Paulissen, E., Vissart, A., 2001. Quaternary lithostratigraphic units (Belgium). Geologica Belgica 4/1–2, 153–164. https://doi.org/10.20341/gb.2014.051

Hatano, N., Yoshida, K., Sasao, E., 2019. Effects of grain size on the chemical weathering index: A case study of Neogene fluvial sediments in southwest Japan. Sedimentary Geology 386, 1–8. https://doi.org/10.1016/j.sedgeo.2019.03.017

Hofer, G., Wagreich, M., Neuhuber, S., 2013. Geochemistry of fine-grained sediments of the upper Cretaceous to Paleogene Gosau Group (Austria, Slovakia): Implications for paleoenvironmental and provenance studies. Geoscience Frontiers 4, 449–468. https://doi.org/10.1016/j.gsf.2012.11.009

Ivanova, V. V., Erbajeva, M.A., Snchetnikov, A.A., Kazansky, A.Y., Matasova, G.G., Alexeeva, N. V., Filinov, I.A., 2019. Tolbogoi key section: A unique archive for Pliocene-Pleistocene paleoenvironment dynamics of Transbaikalia, Bikal rift zone. Quaternary International 519, 58–73. https://doi.org/10.1016/j.quaint.2018.11.004

Johnsson, M.J., 1993. The system controlling the composition of clastic sediments. Special Paper of the Geological Society of America 284, 1–19. https://doi.org/10.1130/SPE284-p1

Kassi, A.M., Grigsby, J.D., Khan, A.S., Kasi, A.K., 2015. Sandstone petrology and geochemistry of the Oligocene-Early Miocene Panjgur Formation, Makran accretionary wedge, southwest Pakistan: Implications for provenance, weathering and tectonic setting. Journal of Asian Earth Sciences 105, 192–207. https://doi.org/10.1016/j.jseaes.2015.03.021

Kemp, D.B., Sadler, P.M., Vanacker, V., 2020. The human impact on North American erosion, sediment transfer, and storage in a geologic context. Nature communications 11, 6012. https://doi.org/10.1038/s41467-020-19744-3

Laloy, E., Beerten, K., Vanacker, V., Christl, M., Rogiers, B., Wouters, L., 2017. Bayesian inversion of a CRN depth profile to infer Quaternary erosion of the northwestern Campine Plateau (NE Belgium). Earth Surface Dynamics 5, 331–345. https://doi.org/10.5194/esurf-5-331-2017

Lauer, T., Weiss, M., Bernhardt, W., Heinrich, S., Rappsilber, I., Stahlschmidt, M.C., von Suchodoletz, H., Wansa, S., 2020. The Middle Pleistocene fluvial sequence at Uichteritz, central Germany: Chronological framework, paleoenvironmental history and early human presence during MIS 11, 107016. Geomorphology 354. https://doi.org/10.1016/j.geomorph.2019.107016

le Dortz, K., Meyer, B., Sébrier, M., Braucher, R., Bourlès, D., Benedetti, L., Nazari, H., Foroutan, M., 2012. Interpreting scattered in-situ produced cosmogenic nuclide depth-profile data. Quaternary Geochronology 11, 98–115. https://doi.org/10.1016/j.quageo.2012.02.020

Mann, H.B., Whitney, D.R., 1947. On a test of whether one of two random variables is stochastically larger than the other. Annals of mathematical statistics 18, 50–60.

McLennan, S., 2001. Relationships between the trace element composition of sedimentary rocks and upper continental crust. Geochemistry Geophysics Geosystems 2, 2000GC000109. https://doi.org/2000GC000109

Miall, A.D., 1996. The geology of fluvial deposits, 1st ed. Springer, Berlin, Germany. https://doi.org/10.1007/978-3-662-03237-4

Mitchell, R.L., Sheldon, N.D., 2016. Sedimentary provenance and weathering processes in the 1.1Ga Midcontinental Rift of the Keweenaw Peninsula, Michigan, USA. Precambrian Research 275, 225–240. https://doi.org/10.1016/j.precamres.2016.01.017

Nesbitt, H.W., Young, G.M., 1982. Early proterozoic climates and plate motions inferred from major element chemistry of lutites. Nature 299, 715-717. https://doi.org/10.1038/299715a0

Nesbitt, H.W., Young, G.M., McLennan, S.M., Keays, R.R., 1996. Effects of chemical weathering and sorting on the petrogenesis of siliciclastic sediments, with implications for provenance studies. Journal of Geology 104 (5), 525-542. https://doi.org/10.1086/629850

Paulissen, E., 1973. De Morfologie en de Kwartairstratigrafie van de Maasvallei in Belgisch Limburg. Verhandelingen van de koninklijke Vlaamse academie voor wetenschappen, letteren en schone kunsten van België. Klasse der Wetenschappen 127,1–266.

Paulissen, E., 1983. Les grappes alluviales et les failles Quaternaires du Plateau de Campine, in: Robaszynski, F., Dupuis, C. (Eds.), Guides Géologiques Régionaux – Belgique. Masson, Paris, France, pp. 167–170.

Retallack, G.J., 1997. A Colour Guide to Paleosols, 1st ed. Wiley-Blackwell, Chichester, United Kingdom.

Retallack, G.J., 2019. Soils of the Past: An Introduction to Paleopedology, 3rd ed. Wiley-Blackwell, Chichester, United Kingdom. https://doi.org/10.1002/9780470698716

Rixhon, G., Bourlès, D.L., Braucher, R., Siame, L., Cordy, J.M., Demoulin, A., 2014. $^{10}$Be dating of the Main Terrace level in the Amblève valley (Ardennes, Belgium): New age constraint on the archaeological and palaeontological filling of the Belle-Roche palaeokarst. Boreas 43, 528–542. https://doi.org/10.1111/bor.12066

Rizza, M., Abdrakhmatov, K., Walker, R., Braucher, R., Guillou, V., Carr, A.S., Campbell, G., McKenzie, D., Jackson, J., Aumaître, G., Bourlès, D.L., Keddadouche, K., 2019. Rate of slip from multiple Quaternary dating methods and paleoseismic investigations along the Talas-Fergana fault:

tectonic implications for the Tien Shan Range. Tectonics 38, 2477–2505. https://doi.org/10.1029/2018TC005188

Schaller, M., von Blanckenburg, F., Hovius, N., Kubik, P.W., 2001. Large-scale erosion rates from in situ-produced cosmogenic nuclides in European river sediments. Earth and Planetary science letters 188, 441-458. https://doi.org/10.1016/S0012-821X(01)00320-X

Schumm, S.A., 1985. Patterns of alluvial rivers. Annual review of Earth and planetary sciences 13, 5-27. https://doi.org/10.1146/annurev.earth.13.1.5

Sheldon, N.D., Tabor, N.J., 2009. Quantitative paleoenvironmental and paleoclimatic reconstruction using paleosols. Earth-Science Reviews 95, 1-52. https://doi.org/10.1016/j.earscirev.2009.03.004

Stange, K.M., van Balen, R., Vandenberghe, J., Peña, J.L., Sancho, C., 2013. External controls on Quaternary fluvial incision and terrace formation at the Segre River, Southern Pyrenees. Tectonophysics 602, 316–331. https://doi.org/10.1016/j.tecto.2013.10.033

Tebbens, L.A., Veldkamp, A., 2000. Late Quaternary evolution of fluvial sediment composition: a modeling case study of the River Meuse, Global and Planetary Change 27, 187-206. https://doi.org/10.1016/S0921-8181(01)00066-2

van den Berg, M.W., 1996. Fluvial sequences of the Maas: a 10 Ma record of neotectonics and climatic change at various time-scales (Doctoral dissertation). University of Wageningen, Wageningen.

Vanacker, V., Ameijeiras-Mariño, Y., Schoonejans, J., Cornélis, J.T., Minella, J.P.G., Lamouline, F., Vermeire, M.L., Campforts, B., Robinet, J., van de Broek, M., Delmelle, P., Opfergelt, S., 2019. Land use impacts on soil erosion and rejuvenation in Southern Brazil. Catena 178, 256–266. https://doi.org/10.1016/j.catena.2019.03.024

Vanacker, V., von Blanckenburg, F., Govers, G., Molina, A., Campforts, B., Kubik, P.W., 2015. Transient river response, captured by channel steepness and its concavity. Geomorphology 228, 234-243. https://doi.org/10.1016/j.geomorph.2014.09.013

Vandenberghe, J., 1995. Timescale, Climate and River Development. Quaternary Science Reviews 14, 631-639. https://doi.org/10.1016/0277-3791(95)00043-O

Vandenberghe, J., 2015. River terraces as a response to climatic forcing: Formation processes, sedimentary characteristics and sites for human occupation. Quaternary International 370, 3–11. https://doi.org/10.1016/j.quaint.2014.05.046

Vandenberghe, J., 2008. The fluvial cycle at cold-warm-cold transitions in lowland regions: A refinement of theory. Geomorphology 98, 275–284. https://doi.org/10.1016/j.geomorph.2006.12.030

Vanneste, K., Verbeeck, K., Camelbeeck, T., Paulissen, E., Meghraoui, M., Renardy, F., Jongmans, D., Frechen, M., 2001. Surface-rupturing history of the Bree fault scarp, Roer Valley graben: Evidence for six events since the late Pleistocene. Journal of Seismology 5, 329–359. https://doi.org/10.1023/A:1011419408419

Varga, A.R., Szakmány, G., 2004. Geochemistry and provenance of the upper carboniferous sandstones from borehole Diosviszlo-3 (Teseny Sandstone Formation, SW Hungary). Acta Mineralógica Petrographica 45, 7–14.

Vauclin, S., Mourier, B., Tena, A., Piégay, H., Winiarski, T., 2020. Effects of river infrastructures on the floodplain sedimentary environment in the Rhône River. Journal of Soils and Sediments 20, 2697–2708. https://doi.org/10.1007/s11368-019-02449-6

Viers, J., Dupré, B., Gaillardet, J., 2009. Chemical composition of suspended sediments in World Rivers: New insights from a new database. Science of the Total Environment 407, 853–868. https://doi.org/10.1016/j.scitotenv.2008.09.053

von Blanckenburg, F., Belshaw, N.S., O'Nions, R.K., 1996. Separation of $^{9}$Be and cosmogenic $^{10}$Be from environmental materials and SIMS isotope dilution analysis. Chemical Geology 129, 93–99. https://doi.org/10.1016/0009-2541(95)00157-3

**Declaration of Competing Interest**

The authors declare that they have no known competing financial interests or personal relationships that could have appeared to influence the work reported in this paper.

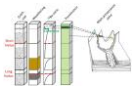

Graphical abstract

Highlights:

- Fluvial dynamics of Pleistocene braided river from northwestern Europe.
- Grain size, chemical weathering and provenance complement $^{10}$Be depth profiles.
- Hiatuses in deposition are identified based on $^{10}$Be depth profiles and grain size.
- Environmental conditions can be reconstructed based on weathering proxies.
- Analysis of provenance allows one to flag samples before $^{10}$Be analyses.

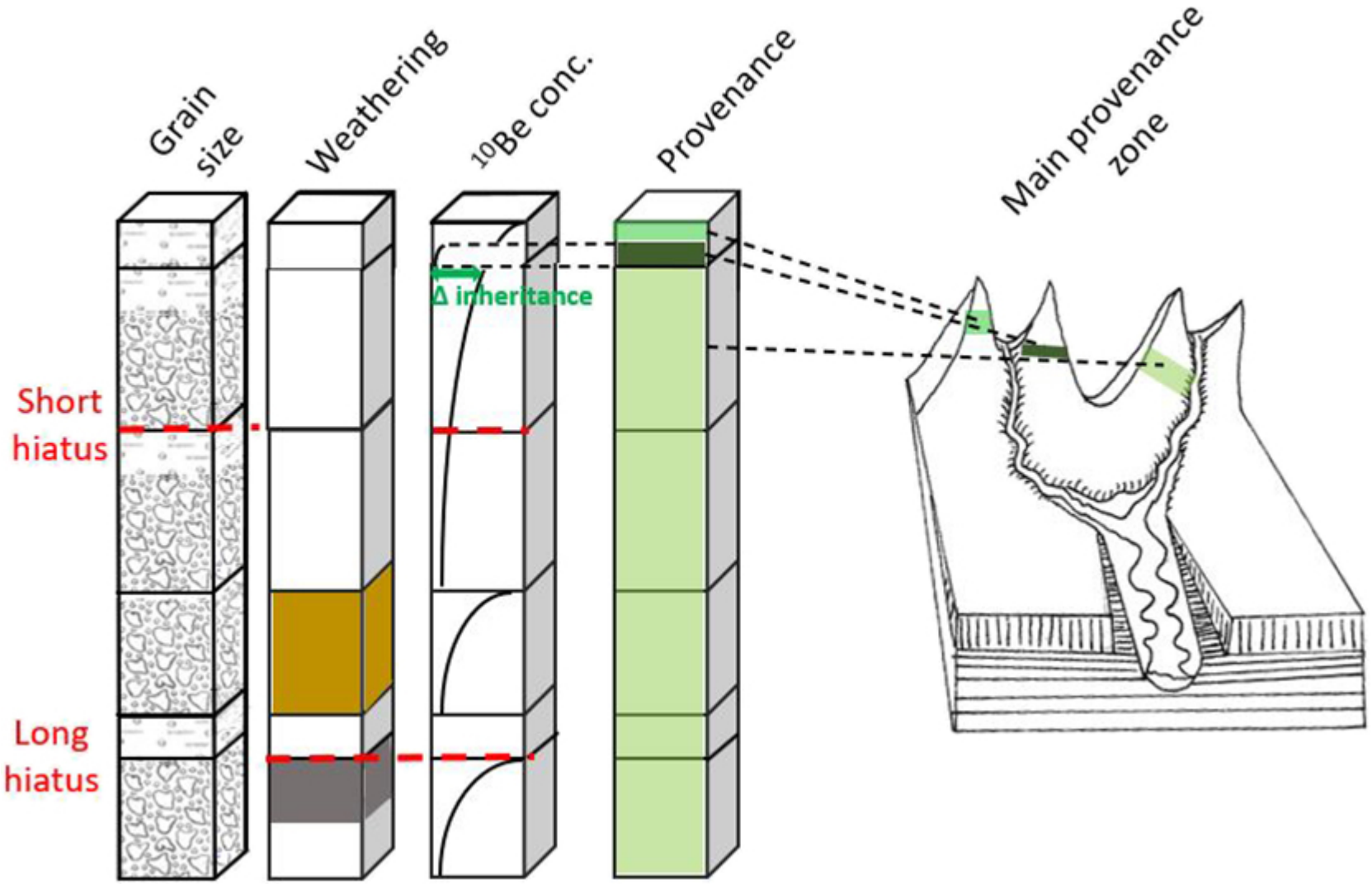


Graphics Abstract

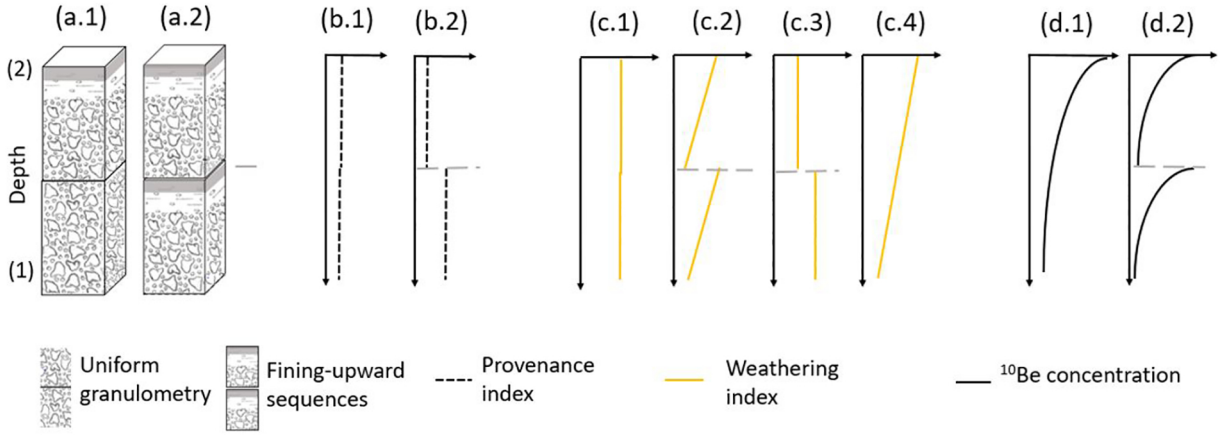
(a.1)
(a.2)
(b.1)
(b.2)
(c.1)
(c.2)
(c.3)
(c.4)
(d.1)
(d.2)
(2)
Depth
(1)
Uniform granulometry
Fining-upward sequences
Provenance index
Weathering index
$^{10}$Be concentration

Figure 1

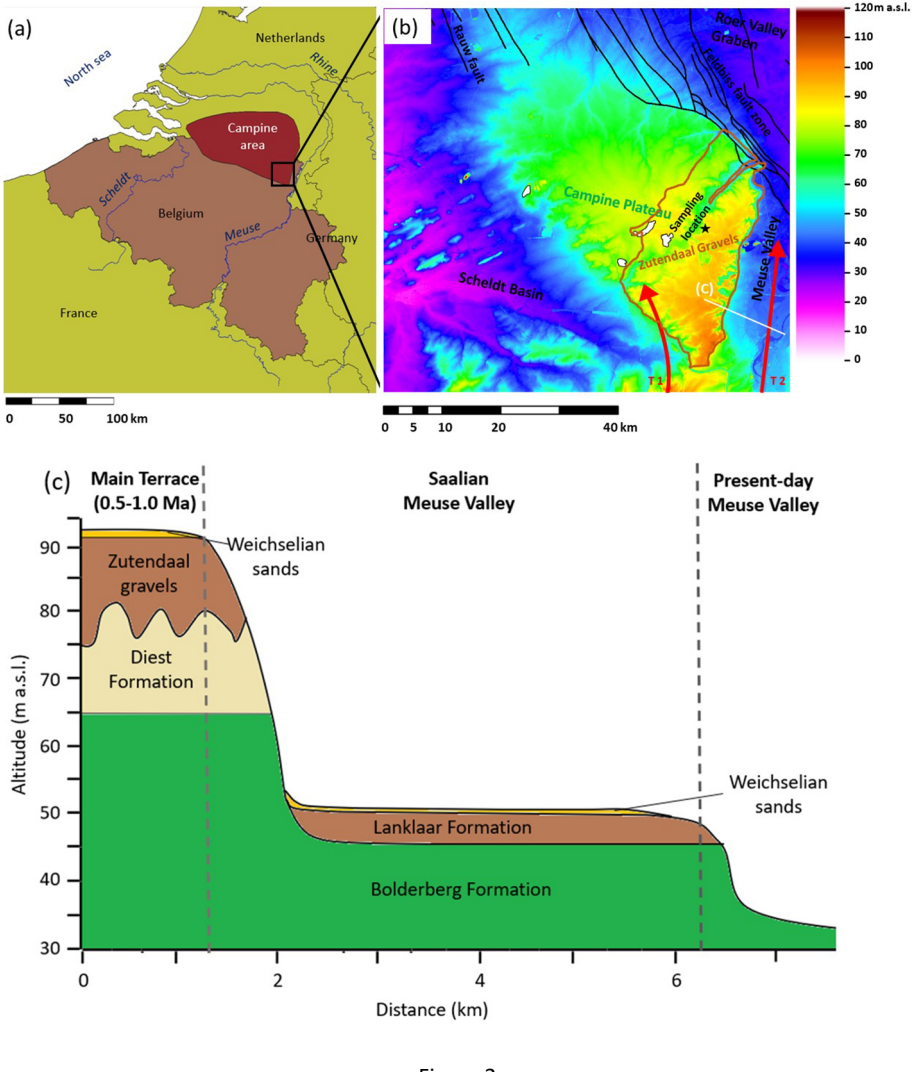
(a)
North sea
Netherlands
Rhine
Campine area
Scheldt
Belgium
Meuse
Germany
France
0 50 100 km
(b)
Raw fault
Roer Valley Graben
Feldbiss fault zone
Campine Plateau
Sampling location
Zutendaal Gravels
Scheldt Basin
(C)
Meuse Valley
T1
T2
120m a.s.l.
110
100
90
80
70
60
50
40
30
20
10
0
0 5 10 20 40 km
(c)
Main Terrace (0.5-1.0 Ma)
Saalian Meuse Valley
Present-day Meuse Valley
Zutendaal gravels
Weichselian sands
Diest Formation
Lanklaar Formation
Weichselian sands
Bolderberg Formation
Altitude (m a.s.l.)
90
80
70
60
50
40
30
0
2
4
6
Distance (km)

Figure 2

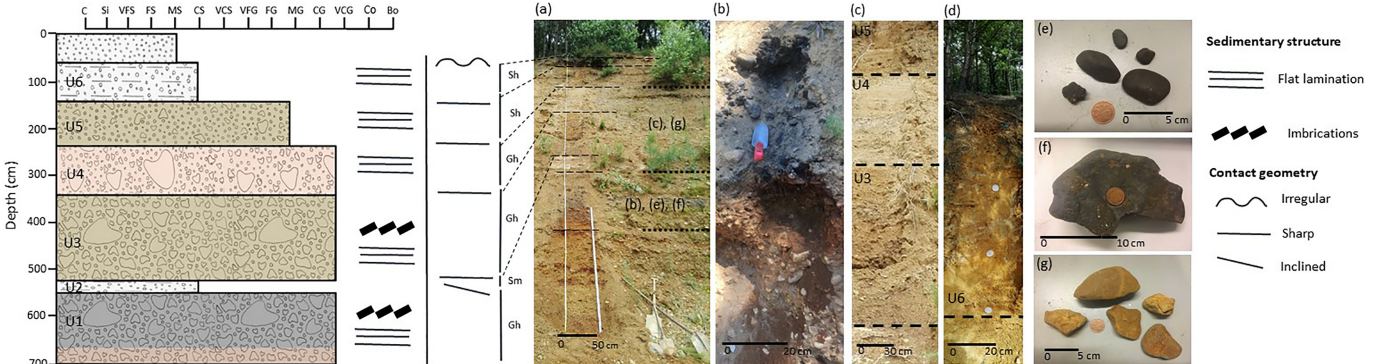
C Si VFS FS MS CS VCS VFG FG MG CG VCG Co Bo
Depth (cm)
0
100
200
300
400
500
600
700
U6
U5
U4
U3
U2
U1
Sh
Sh
Gh
Gh
Sm
Gh
(a)
(c), (g)
(b), (e), (f)
0 50 cm
(b)
0 20 cm
(c)
U5
U4
U3
0 30 cm
(d)
U6
0 20 cm
(e)
0 5 cm
(f)
0 10 cm
(g)
0 5 cm
Sedimentary structure
Flat lamination
Imbrications
Contact geometry
Irregular
Sharp
Inclined

Figure 3

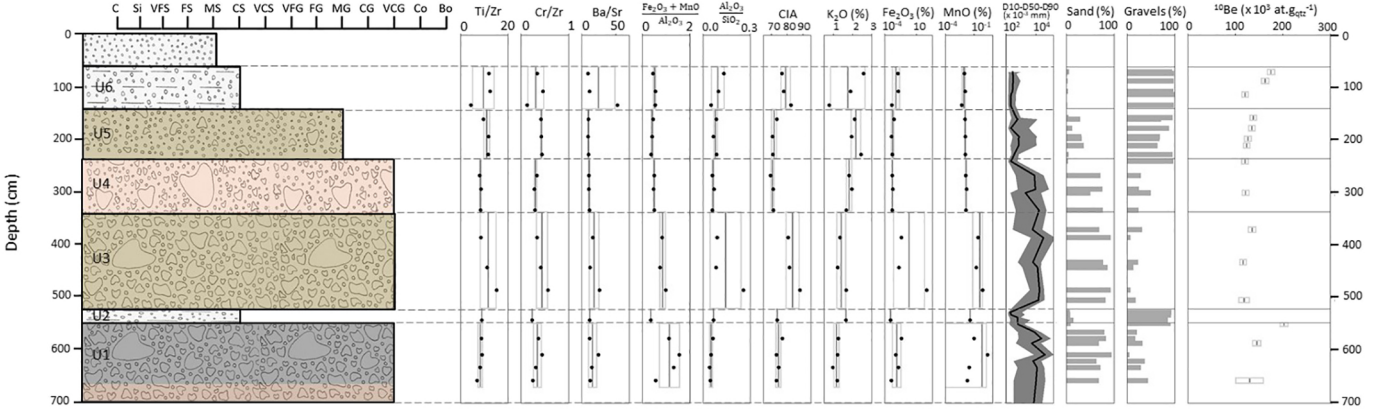
C Si VFS FS MS CS VCS VFG FG MG CG VCG Co Bo
Depth (cm)
U6
U5
U4
U3
U2
U1
Ti/Zr
Cr/Zr
Ba/Sr
Fe2O3 + MnO / Al2O3
Al2O3 / SiO2
CIA
K2O (%)
Fe2O3 (%)
MnO (%)
D10-D50-D90 (x10-3 mm)
Sand (%)
Gravels (%)
10Be (x 10³ at.gqtz-1)

Figure 4

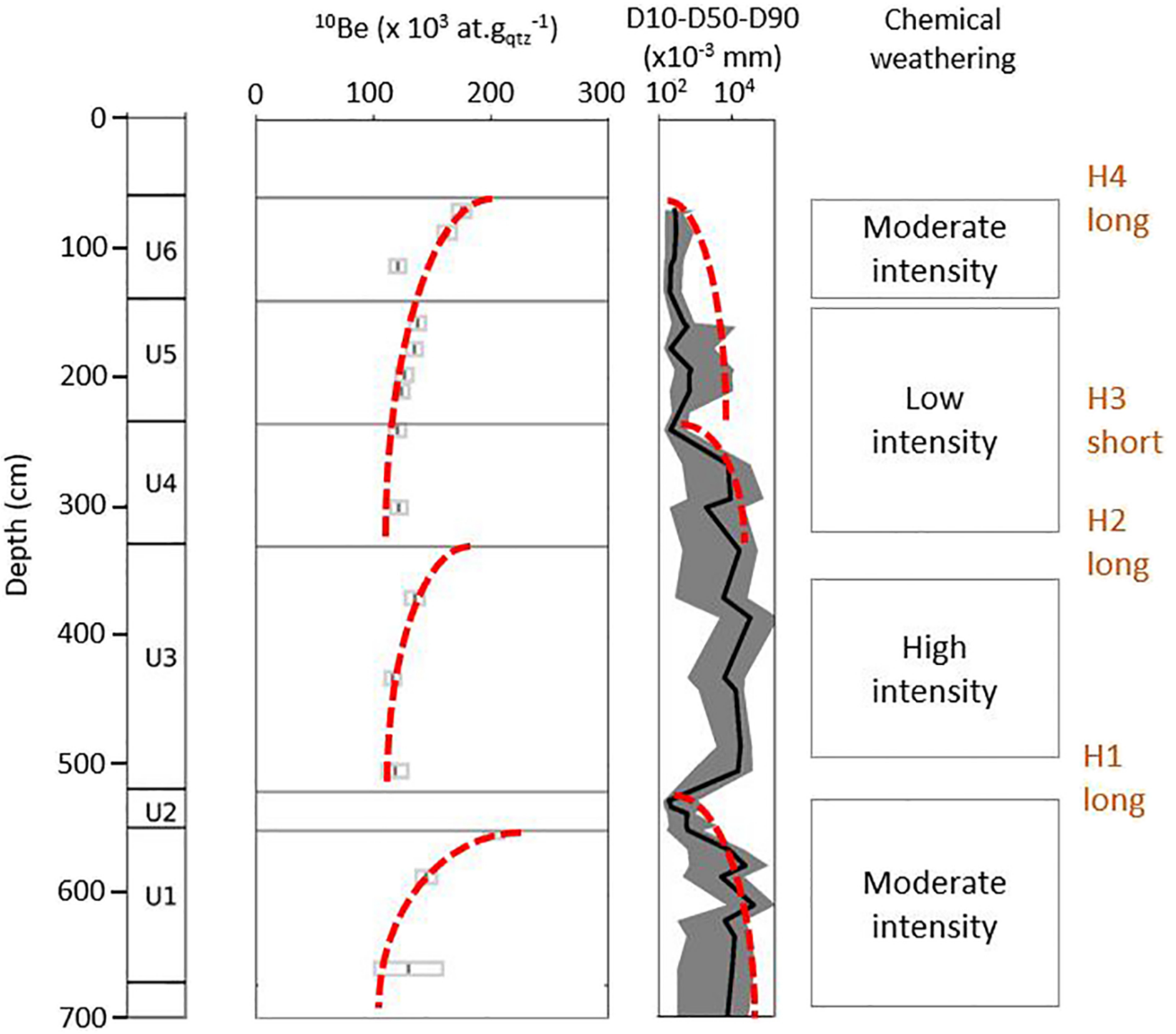
$^{10}$Be (x 10$^3$ at.g$_{qtz}^{-1}$)
0
100
200
300
D10-D50-D90
(x10$^{-3}$ mm)
10$^2$
10$^4$
Chemical weathering
Depth (cm)
0
100
200
300
400
500
600
700
U6
U5
U4
U3
U2
U1
Moderate intensity
Low intensity
High intensity
Moderate intensity
H4 long
H3 short
H2 long
H1 long

Figure 5

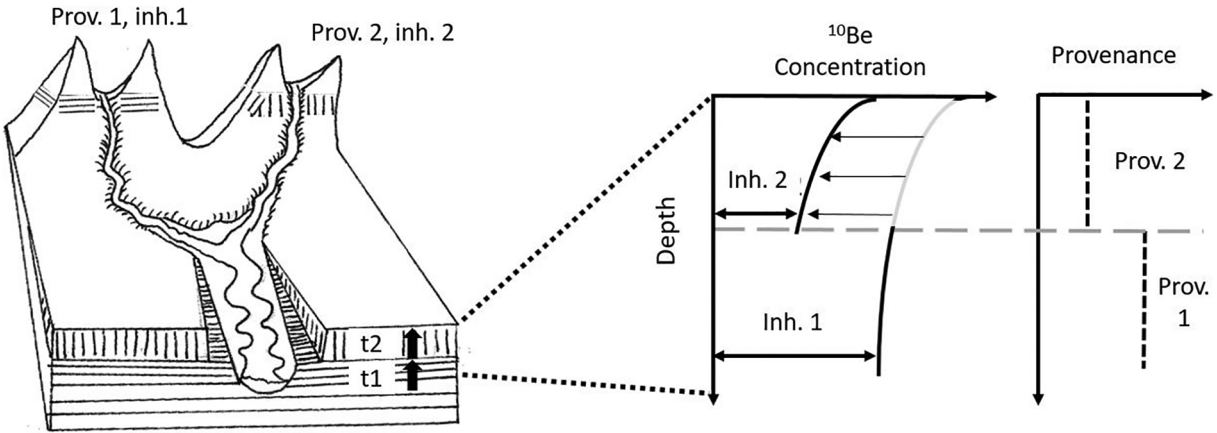
Prov. 1, inh.1
Prov. 2, inh. 2
t2
t1
$^{10}$Be
Concentration
Provenance
Depth
Inh. 2
Inh. 1
Prov. 2
Prov.
1

Figure 6